

Multispectral surface emissivity from VIRTIS on Venus Express

N.T. Mueller^{a,b,*}, S.E. Smrekar^a, C.C.C. Tsang^c

^a*Jet Propulsion Laboratory, California Institute of Technology, 4800 Oak Grove Drive, Pasadena, CA 91109 USA*

^b*Now at the German Aerospace Center (DLR) Institute for Planetary Research, Rutherfordstr 2, 12489 Berlin, Germany*

^c*Department of Space Studies, Southwest Research Institute, Boulder, CO 80302 USA*

Abstract

The surface composition of Venus is mostly inaccessible to remote observation due to the dense cloud cover. There are five spectral windows that show measurable thermal emission from the surface at night. The VIRTIS spectrometer on Venus Express observed three of these windows over much of the southern hemisphere of Venus. We use these data along with Magellan altimetry to map surface emissivity. The data are initially processed to correct for instrumental straylight from the dayside of Venus and to improve wavelength registration. These corrected data are then inverted to emissivity at 1020, 1100, and 1180 nm wavelength using lookup tables created by an atmospheric radiative transfer model. As in earlier studies we find residual trends of surface emissivity with respect to the Magellan altimetry that is used in the model to determine surface temperature and thickness of the atmosphere. A new observation is that these trends vary significantly from region to region, indicating some lateral variability of atmospheric parameters, most likely near surface atmospheric temperature. The trends are consistent over hundreds to thousands of km, thus it is possible to correct for them heuristically. In two regions studied in this paper there are significant deviations from the background emissivity which are associated with some geologic features. The high noise in 1100 and 1180 nm maps derived from VIRTIS data result in large uncertainties of spectral shape. The VIRTIS instrument was not designed for this task and future observations could provide high signal to noise ratio maps in at least 5 distinct bands diagnostic of major rock types and minerals.

© 2018. All rights reserved.

1. Introduction

The surface composition of Venus is not well known. There are in-situ measurements at a number of landing sites and indirect evidence from the surface morphology observed by radar, but many of the most useful remote sensing methods for surface composition are prohibited by the dense atmosphere and complete cloud cover. There are several near infrared spectral windows that allow us to observe surface thermal emission on the dark side of the planet (Carlson et al., 1991; Lecacheux et al., 1993; Baines et al.,

*Corresponding author

2000). With suitable atmospheric corrections, these observations provide some constraints on Venus surface composition in comparison with laboratory data (Helbert et al., 2018).

The instrument VIRTIS (Visible InfraRed Thermal Imaging Spectrometer) on the Venus Express orbiter (Piccioni et al., 2007) observed surface thermal emission at three of the spectral windows, centered at 1020, 1100, and 1180 nm wavelength. The thermal emission is foremost a function of surface elevation, because surface temperature is dominated by atmospheric temperature which does not show large diurnal or latitudinal variations but increases with depth of the atmosphere (Seiff et al., 1985).

Mueller et al. (2008) used this correlation to produce a map of observed 1020 nm thermal emission relative to the global average as a function of Magellan radar altimetry (Ford and Pettengill, 1992). This provides a map of relative variations of emissivity, although the relation to absolute emissivity is not clear without deeper understanding of the radiative transfer within the atmosphere of Venus (Hashimoto and Sugita, 2003; Arnold et al., 2008). The map shows some plausible correlation with geological features identified in Magellan radar images and has been interpreted in terms of relative weathering age (Helbert et al., 2008; Smrekar et al., 2010; Stofan et al., 2016; D’Incecco et al., 2017) and primary rock composition (Mueller et al., 2008; Gilmore et al., 2015). This statistical method is less useful for the 1100 nm and 1180 nm windows due to steeper spectral gradients and variations in the spectral calibration of VIRTIS.

Several studies have applied radiative transfer models to derive surface emissivity from near infrared spectra and images (Meadows and Crisp, 1996; Hashimoto et al., 2008; Basilevsky et al., 2012), but this approach has not yet been used with the whole VIRTIS dataset. Kappel (2014) has developed a method to fit multiple spectra simultaneously by iterating a numerical radiative transfer model to separate atmospheric parameters from surface emissivity. The method involves that all spectra of the same surface should be modeled with the same surface emissivity while atmospheric parameters are variable but correlated in space and time. The method of Kappel (2014) is limited by computational feasibility to small regions and subsets of the VIRTIS data set, such Themis Regio between -46°N to 36°N and 270°E to 288°E in the work of Kappel et al. (2016).

We aim to develop a method also based on radiative transfer but which allows for processing of all VIRTIS data with a consistent solution that relates observed radiances to surface emissivity. While this cannot as accurately account for atmospheric variables as the method by Kappel (2014), it can provide global emissivity maps in the three windows observed by VIRTIS.

2. Atmospheric radiative transfer

To derive emissivity we use lookup tables of Venus thermal emission radiance spectra calculated by the atmospheric radiative transfer model created by Tsang et al. (2008) based on the work of Kamp et al. (1988) and Irwin (1997). The model assumes a plane parallel atmosphere and includes atmospheric absorption,

emission and multiple scattering at molecules and cloud droplets, with more details on how these affect the lookup table in the following subsections. The atmosphere model lower boundary is set at various pressure levels, sampling the range of elevation of the surface observed by VIRTIS.

The thermal emission originating at the lower boundary of the model is defined by surface temperature and surface emissivity, a parameter that is indicative of chemical composition and surface texture. The surface emissivity is defined as the ratio of emitted thermal emission radiance to the blackbody radiance of the surface temperature. The surface is assumed to be at the same temperature as the atmosphere of that altitude (Lecacheux et al., 1993). The surface is further modeled as reflecting downwelling radiation according to Kirchhof’s Law, i.e. $e = 1 - r$, where r is surface reflectivity and e is surface emissivity.

The lookup table has 5 dimensions in total, representing variation in 1. wavelength (1000 to 1350 nm at 1 nm resolution), 2. surface emissivity (0.2 to 1.0), 3. surface elevation (-2 to 6 km), 4. CO₂ collision induced absorption (CIA) coefficient (0.1×10^{-9} to 3×10^{-9} cm⁻¹amagat⁻²), and 5. cloud opacity (22 to 70).

2.1. Atmosphere temperature and pressure profile

Atmospheric temperatures and pressures are as described in the Venus International Reference Atmosphere (VIRA) (Seiff et al., 1985), which is mostly extrapolated from the four Pioneer Venus descent profiles. The model extends to 735.3 K at 0 km altitude, which corresponds to a radius of 6052 km. For lower surface elevations we extrapolate the temperature and pressure to 750.5 K and 103.42 bar at -2 km altitude, and 742.9 K and 97.77 bar at -1 km. The lapse rate is approximately -7.6 K/km.

Some previous studies aiming to derive emissivity (Meadows and Crisp, 1996; Mueller et al., 2008; Basilevsky et al., 2012) refer to the near surface adiabatic lapse rate of -8 K/km given by Seiff et al. (1985) in their table 1-1, column 6. Calculations of the adiabatic lapse rate as ratio of gravity (8.87 m/s² Colin, 1983) to specific heat capacity at constant pressure (Lebonnois and Schubert, 2017, Table S1), as well as the Venus gravity of give adiabatic lapse rates of -7.4 K/km to -7.6 K/km in the near surface pressure range of 100 to 70 bar.

The VeGa 2 lander descent data is the highest resolution temperature profile near the surface and shows different, higher lapse rate which appears to be unstable below 6 km, (Seiff, 1987; Young et al., 1987). Lebonnois and Schubert (2017) propose density driven separation of N₂ in the layer of supercritical CO₂ which could explain the high temperature lapse rate indicated by the VeGa 2 profile. The analysis of near infrared data by (Meadows and Crisp, 1996) on the other hand indicates a lower lapse rate than in the VIRA model for the atmosphere in contact with the surface. We use the VIRA profile to maintain comparability with previous work using that thermal structure (e.g. Hashimoto et al., 2008; Basilevsky et al., 2012; Kappel et al., 2016).

2.2. Gaseous absorption

Gaseous absorption of CO₂ and seven trace gas species is modeled based on line databases HITRAN (Rothman et al., 2003) and HITEMP (Rothman et al., 2010). Abundances of these gaseous constituents are constant in this work. Of the minor species only H₂O has a large impact on the surface windows, but no significant variation has been reported so far (Bézard et al., 2009) and we adopt a constant value of 35 ppm, similar to the value derived by Bézard et al. (2011). The details of absorption line shape are as in the work of (Tsang et al., 2008). We add CO₂ CIA as a binary absorption coefficient as discussed by Pollack et al. (1993). The value of this CIA parameter is not well known from laboratory data (Stefani et al., 2013; Snels et al., 2014b,a) and we model the lookup tables for several values, effectively making this one of the dimensions of the lookup table.

2.3. Cloud model

In some of the spectral windows, e.g. at 1310 nm, 1740 nm, and 2300 nm, the radiance purely originates from the atmosphere between cloud layer and surface, which can be used to correct the surface windows between 800 and 1200 nm for cloud opacity (Meadows and Crisp, 1996; Hashimoto et al., 2008; Mueller et al., 2008; Haus and Arnold, 2010; Kappel et al., 2012; Kappel, 2014; Kappel et al., 2015, 2016; Mueller et al., 2017).

The optical properties of the cloud particles change significantly between these wavelength regions (e.g. Grinspoon et al., 1993), and the extrapolation from the 1740 and 2300 nm band to the surface windows is susceptible to the assumptions on cloud parameters (e.g. Kappel et al., 2015). The 1310 nm atmospheric window is however closer to the surface windows in wavelength and thus its cloud opacity is more similar to the surface windows. Using only the 1310 nm window to constrain cloud opacity does not result in excessive errors in retrieved surface emissivity (Kappel et al., 2015). In the VIRTIS data, this window has lower signal to noise than the 1740 and 2300 nm windows and is more susceptible to solar straylight, but our method of using lookup tables is greatly simplified by using only one single parameter representing the clouds, constrained by a single band.

We model the clouds similar to the work by Barstow et al. (2012), based on the model by Tsang et al. (2008), with four distinct particle size populations defined by modal radius and radius variance as derived by Crisp (1986) from various remote and in-situ observations. The nominal vertical profile of number density of the different modes is shown in Fig. 1. To simulate the variable optical thickness of the clouds we multiply the density of the two largest cloud modes, 2' and 3 (Crisp, 1986), with the same factor. Systematic variation of this factor provides the final dimension of the lookup table.

Kappel et al. (2015) evaluate the impact of cloud particle size distribution variations on emissivity derivation when cloud opacity is only determined from 1310 nm observations. For a single spectrum the error resulting from a 25 % density variation relative to the assumed value in each of the four particle modes is 5%,

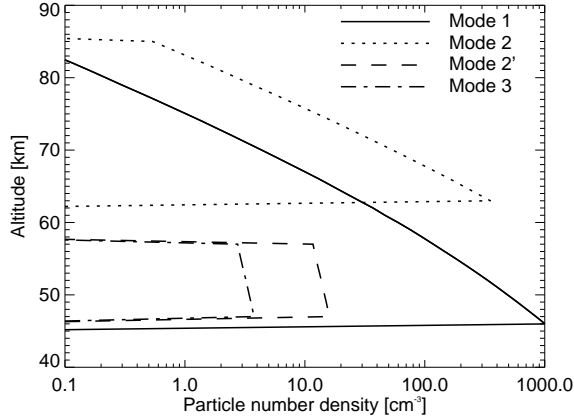


Figure 1: Cloud model number densities for the different size modes. We model the variability of the clouds by multiplying the number density of cloud modes 2' and 3 by the same factor.

15%, and 10% for the 1020 nm, 1100 nm and 1180 nm windows respectively. When averaging over at least 100 VIRTIS images as in the locations studied here, the error should be reduced by an order of magnitude, unless the errors are non-random. There could conceivably be changes in the cloud properties that are tied to geographical location as there are standing gravity waves manifesting as temperature deviations of a few K at the cloud tops above some highlands (Fukuhara et al., 2017). However these standing gravity waves have only been observed at highlands with elevations above 3 km, and notably not at the highlands Alpha and Phoebe Regios (Kouyama et al., 2017), which are in the vicinity of our study regions. The bow shaped anomalies associated with the observed gravity waves would not extend into the two study regions. In case there were an anomaly in cloud opacity associated with these features, mapping of cloud opacity in geographical coordinates would reveal this.

3. Data and its preparation

3.1. Magellan altimetry

We use radar altimetry data from the Magellan mission with a spatial resolution of approximately 20×10 km² (Ford and Pettengill, 1992) at the southern latitudes imaged by VIRTIS. The data were updated with improved Magellan ephemeris and projected on a 5×5 km² grid by Rappaport et al. (1999), in the same format as the Magellan Global Topography Data Record (GTDR) archived on the National Aeronautics and Space Administration (NASA) Planetary Data System (PDS).

The radiative transfer through the atmosphere of Venus up to the cloud tops is a diffusive process and therefore the instrument line of sight (LOS) intersect with the cloud level represented by a 6111 km sphere

provides the appropriate coordinate referencing (Erard et al., 2009). The topography data is referenced to VIRTIS spectra footprints with a shift in longitude of 0.15° , which aligns the two data sets in a minimum chi square sense in the cartographic coordinate system given by Seidelmann et al. (2005), and is consistent with the uncertainty of the average spin rate of the planet (Mueller et al., 2012).

Unlike many previous studies that use derived emissivity (Helbert et al., 2008; Mueller et al., 2008; Mueller et al., 2012; Mueller et al., 2017; Smrekar et al., 2010; Kappel et al., 2012, 2016; Gilmore et al., 2015; Stofan et al., 2016; D’Incecco et al., 2017) we do rely on a reduced resolution topography that takes scattering in the cloud layer into account, but instead use the topography at the resolution of the sinusoidal projection GTDR in the inversion to emissivity (as described in section 4.3.1). We prepare a set of reduced resolution topography values associated with the VIRTIS data of the three windows for visualization and further refinement.

3.2. VIRTIS data

VIRTIS is an instrument with three different channels, mapping visible (M-VIS), mapping infrared (M-IR) and high resolution infrared (H). We use the M-IR channel which is a line scanning imaging spectrometer observing in the near infrared from approximately $1\ \mu\text{m}$ to $5\ \mu\text{m}$. The data are organized in three dimensional cubes with the dimensions *band* b , created by spectral dispersion of light across the detector, *sample* s as the spatial direction along the instruments slit, and *line* l , created by the movement of a scanning mirror between readouts of the detector. The data of one instantaneous readout are called a *frame*, an array with dimensions of 256 samples and 431 bands. In this study we only use bands 0 to 39 which cover approximately the range of 1020 nm to 1400 nm with a spectral sampling of 9.5 nm.

The calibrated VIRTIS cubes show some artifacts that have to be corrected before interpreting the thermal emission. In these corrections we follow the approach of Kappel et al. (2012). These artifacts are illustrated in Fig. 2. All VIRTIS images are to some extent impacted by straylight owing to the mapping observations orbital geometry above the south pole. Spectra of the nightside (a) show the peaks of surface emission, but are offset by a variable amount of straylight originating from the dayside and scattered within the instrument. Towards the dayside (b), sunlight scattered within the atmosphere beyond the terminator increasingly overwhelms the thermal emission. Space (c) should be dark if not for instrumental straylight. Normalized at band 4, its shape fits well to the lower envelope of the nightside spectrum. Band 4 has negligible thermal emission and can be used as a measure of straylight. The spectral shape and slope of the instrumental straylight is variable.

Most of the time, variation is subtle but in case that the straylight originates within the instantaneous field of view, i.e. if there is dayside within the same line, the effect is obvious. In Fig. 2, spectrum d), on the same line as the dayside, shows a very different relative spectral slope from spectrum c), next to the nightside. Spectra with dayside in the same line are excluded from the dataset and we derive the spectral

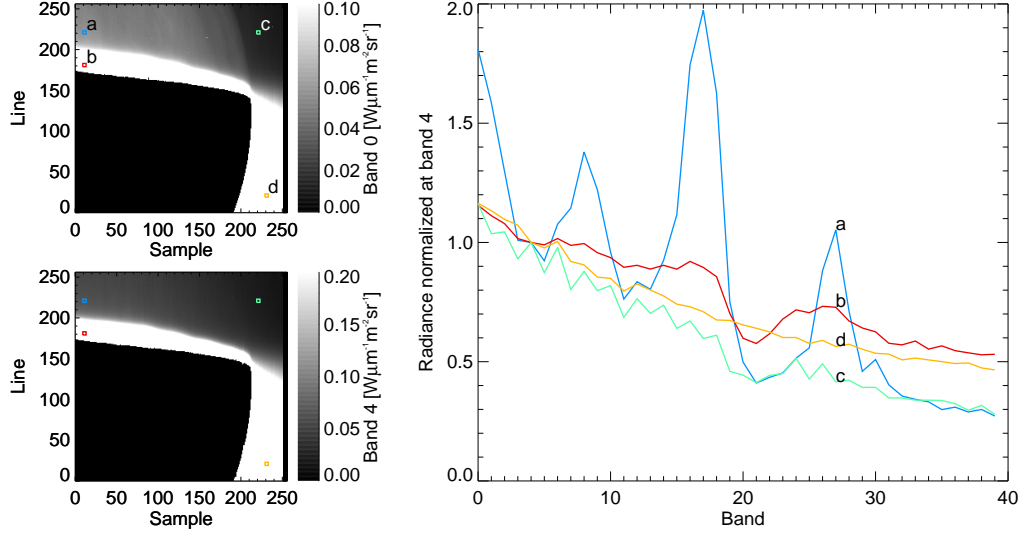


Figure 2: VIRTIS M-IR calibrated data cube VI0025_03 imaging the southern hemisphere of Venus. Shown are bands A) 0 and B) 4 and C) selected spectra scaled by division with their radiance at band 4, where negligible thermal emission is expected. The different spectra are described in the text.

shape of straylight from all spectra showing space similar to c). Prior to straylight removal we need to correct for some detector nonlinearity that manifests as an offset alternating in sign between even and odd bands, i.e. the saw-tooth pattern in Fig.2 spectrum c), in the following called even odd (EO) effect.

We first correct the EO effect following the approach of Kappel et al. (2012) for each detector pixel individually. More details are in the Appendix, section AppendixA.1. We then correct the EO corrected spectra for straylight, also following the principal component analysis approach of Kappel et al. (2012). We note that we find somewhat different spectral shapes of the straylight, possibly a result of a different data selection. More details are in the Appendix, section AppendixA.2. Finally we revise the spectral calibration of the instrument in comparison with our radiative transfer model spectra as in the work of Bézard et al. (2009) and others. This, simply put, shifts the VIRTIS spectra in wavelength and degrades the spectral resolution of the model spectra to find a good fit. More details are in the Appendix, section AppendixA.3. The whole process is illustrated in Fig. 3. The band center wavelengths are affected by position on the detector and instrument temperature, and these changes in wavelengths have to be accounted for when interpreting the data.

We use the whole VIRTIS-M IR dataset of science case 2 and 3 observations (Titov et al., 2006) and select different subsets for each processing step. For the EO correction curve derivation we use all cubes with 0.36 sec exposure duration and full spatial resolution, i.e. 256 samples. From these cubes we select the

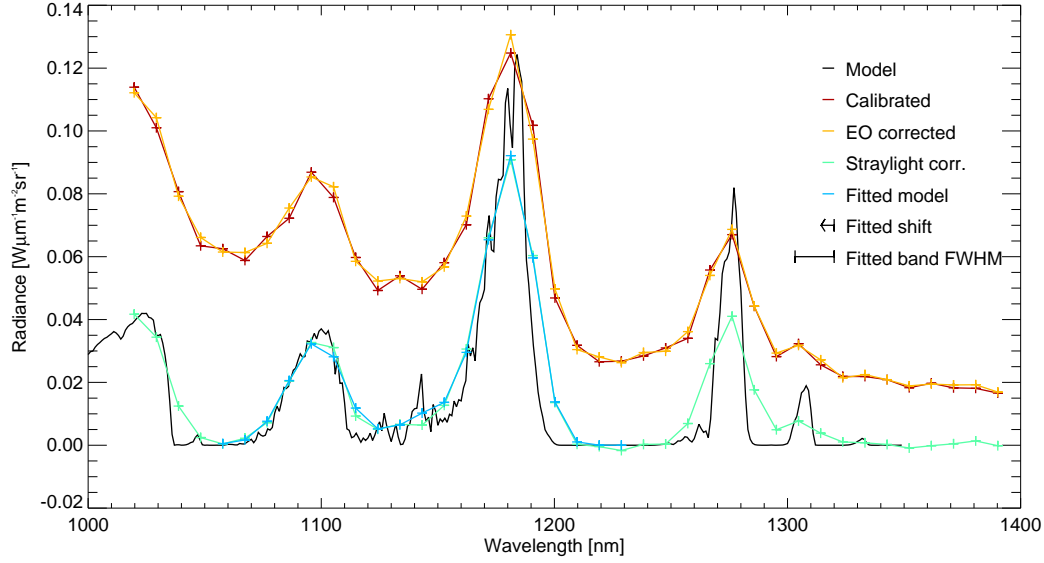


Figure 3: The spectral calibration update fits the EO and straylight corrected spectra individually with synthetic radiances at bands 4 to 19, allowing a shift in wavelengths relative to the ground calibration and the band full width at half maximum (FWHM) as free parameters. Shown for comparison are the calibrated (red), EO corrected (orange), straylight corrected (green) versions of the spectrum a) in Fig.2. The VIRTIS data spectra are shifted in wavelength by approximately 8 nm. The model spectrum at 1 nm resolution is shown in black, the model with bandwidth FWHM of 16 nm is shown in blue.

spectra of the planet with an solar incidence angle less than 93° that are not saturated and do not show signs of excessive noise.

For the derivation of the straylight correction spectral shapes we use 3.3 sec exposure cubes with full spatial resolution showing some deep space next to the planet. From these we select spectra showing space from cubes *lines* that do not also show the dayside of the planet. To provide a representative and relatively noise free base for the principal component analysis, the spectra are further required to have a radiance of at least $0.01 \text{ W}\mu\text{m}^{-1}\text{m}^{-2}\text{sr}^{-1}$ in all bands, less than $0.15 \text{ W}\mu\text{m}^{-1}\text{m}^{-2}\text{sr}^{-1}$ in the first band, and to have between the different bands a standard deviation of less than $0.03 \text{ W}\mu\text{m}^{-1}\text{m}^{-2}\text{sr}^{-1}$.

For the derivation of surface emissivity we use all cubes with at least 3 sec exposure duration and 'reversible' compression. From these cubes we select spectra showing the nightside of a planet with no dayside in the same exposure, i.e. the same line. Further we exclude twilight by restricting spectra to a solar incidence angle greater than 100° , and limit the emission angle to less than 70° .

4. Data inversion

The general approach is to compare the corrected radiances to a lookup table of synthetic radiances calculated by the atmospheric radiative transfer model, to find the set of model parameters that matches the data. We found it practical to correct the observed data stepwise for those parameters that affect the radiance with little interference from each other. These parameters are emission angle, cloud opacity and bandwidth. The former two corrections are analogous to the limb darkening and cloud opacity corrections used by [Mueller et al. \(2008\)](#), but in this work based on the radiative transfer model.

The last step in the data inversion corresponds to the topography and band center wavelength correction in the work of [Mueller et al. \(2008\)](#). The Magellan topography is used to define the surface pressure and temperature boundary conditions for the radiative transfer model based on the VIRA model ([Seiff et al., 1985](#)).

4.1. Clouds

4.1.1. Limb darkening correction

Limb darkening is governed by the extinction scale height in the uppermost cloud layer. We use synthetic radiances calculated at various emission angles to derive a function that scales each window peak radiance to the value it would have at nadir. In our model the upper cloud opacity and scale height does not change and therefore the modeled limb darkening is the same everywhere.

This assumption is justified by in-situ data ([Ragent et al., 1985](#)) and Galileo infrared image analysis ([Grinspoon et al., 1993](#)), which located the variability of the clouds mostly in the lower layer. The variable cloud top altitude at polar latitudes (e.g. [Haus et al., 2014](#)) suggests the possibility of cloud scale height changes, but these latitudes are observed at low emission angles where the limb darkening effect is small. The synthetic limb darkening curves are similar to the linear limb darkening function used by [Mueller et al. \(2008\)](#):

$$\frac{I(\xi)}{I(1)} = 0.31 + 0.69\xi \quad (1)$$

where ξ is the cosine of the emission angle and thus $I(1)$ is the nadir radiance. The ratio of the synthetic limb darkening to this linear curve for the bands used in this study is shown in Fig. 4.

We normalize the synthetic radiances of each window peak to unity at $\xi = 1$ to derive a phase function sampled at several emission angles. To correct for the limb darkening we divide the observed window peak radiance by the value of the corresponding function spline-interpolated to the ξ of each VIRTIS footprint.

4.1.2. Cloud opacity

Cloud opacity is derived from the radiance of the band near 1310 nm. The thermal emission in this window originates from the atmosphere from 10 to 30 km altitude and therefore has no sensitivity to surface

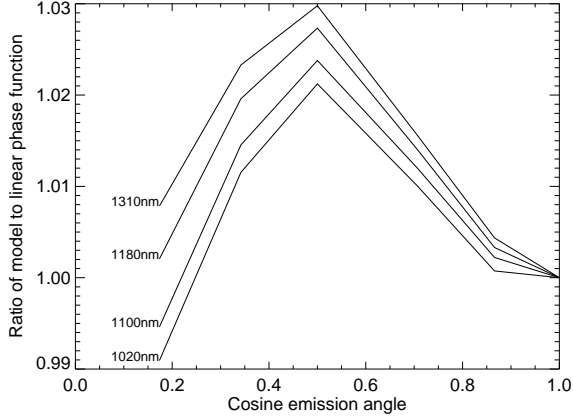


Figure 4: Synthetic radiances as a function of emission angle show a small deviation from the linear simplification of (Mueller et al., 2008) given in Eq. 1 for the four windows used in this study.

topography, temperature, and emissivity (Tsang et al., 2008). The modeling of the 1310 nm radiance has some ambiguity as neither the CO₂ continuum opacity nor the average cloud opacity is known exactly.

To constrain that problem we calculate the median band 30 radiances in bins with increments of 1 nm wavelength and 0.5 nm bandwidth. The distribution of data and contours of the median radiance are shown in Fig. 5. We found that the model radiances (at constant cloud opacity) fit better to the data median if the wavelength of band 30 is shifted by +1.5 nm. Since this wavelength has already been shifted by approximately -8 nm relative to the ground calibration, this might indicate that the synthetic spectrum we used for this correction (Section AppendixA.3) has some systematic deviation from the true spectrum, possibly due to small inaccuracies of the line data base (e.g. Bézard et al., 2009; Haus and Arnold, 2010; Bézard et al., 2011; Kappel, 2014).

Solid contours represent the median observed band 30 radiance in 0.5 nm bandwidth FWHM by 1 nm wavelength bins. Dashed contours represent synthetic radiances with cloud density factor of 1.8 and CIA coefficient of $10^{-10}\text{cm}^{-1}\text{amagat}^{-2}$. The gray scale indicates the amount of data per bin.

The result of the data inversion is the factor that has to be multiplied to the cloud particle number densities of the size modes 2' and 3 shown in Fig. 1 to match data and model radiances. If we select a CIA coefficient (Bézard et al., 1990) of $1 \times 10^{-10}\text{cm}^{-1}\text{amagat}^{-2}$, the average cloud density factor is 1.9. This corresponds to an average cloud optical thickness of 32.3 at 1 μm wavelength. This is somewhat lower than the results based on 1.74 and 2.3 μm radiances presented by Haus et al. (2014).

We find that changes in the continuum coefficient do not provide sufficient leverage to match the results of Haus et al. (2014). The derived cloud opacities show a strong anti-correlation to the intensity of removed straylight in the polar regions below 75°S, which is likely an artifact due to the proximity of the terminator.

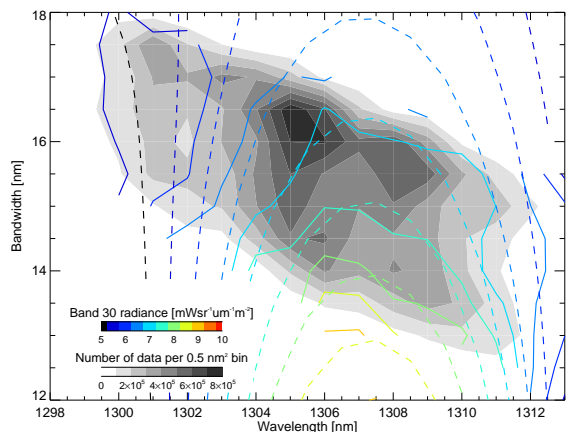


Figure 5: Solid contours represent the median observed band 30 radiance in 0.5 nm bandwidth FWHM by 1 nm wavelength bins. Dashed contours represent synthetic radiances with cloud density factor of 1.8 and CIA coefficient of $10^{-10} \text{ cm}^{-1} \text{ amagat}^{-2}$. The gray scale indicates the amount of data per bin. A shift of 1.5 nm is applied to the wavelength of the bin centers to better align data and model.

We do not interpret these regions.

4.1.3. Cloud opacity correction

In order to simplify the inversion to emissivity we correct the observed surface window radiances to the values they would have at uniform cloud opacity equivalent to the average cloud opacity of 32.3. We define a correction function as the ratio of model radiances to the radiance at average opacity I_c . The correction curve is plotted in Fig. 6 in comparison to data from a narrow interval of the parameter space, all scaled to the average I_c in that interval.

The correction curve shows only negligible variation with parameters other than optical depth. We derive correction curves for each location in the parameter space relevant for VIRTIS observations, which is spanned by topography (-1.5 km to 3.5 km), bandwidth FWHM (13 nm to 18 nm), emissivity (0.2 to 1) and wavelength ranges of 1009 nm to 1024 nm, 1085 nm to 1100 nm, and 1171 nm to 1186 nm for the three bands closest to the window peaks. The variation between all these curves is indicated by error bars in Fig. 6. As a simplification we use the correction curve of the mean data location in the parameter space for the whole parameter space. The observed radiances are divided by the value of the correction curve in Fig. 6 for the appropriate cloud opacity.

4.2. Bandwidth correction

The effective bandwidth of the instrument affects the observed radiance. The effect is small compared to that of cloud opacity and radiometric noise. We correct for bandwidth in a similar manner as cloud opacity.

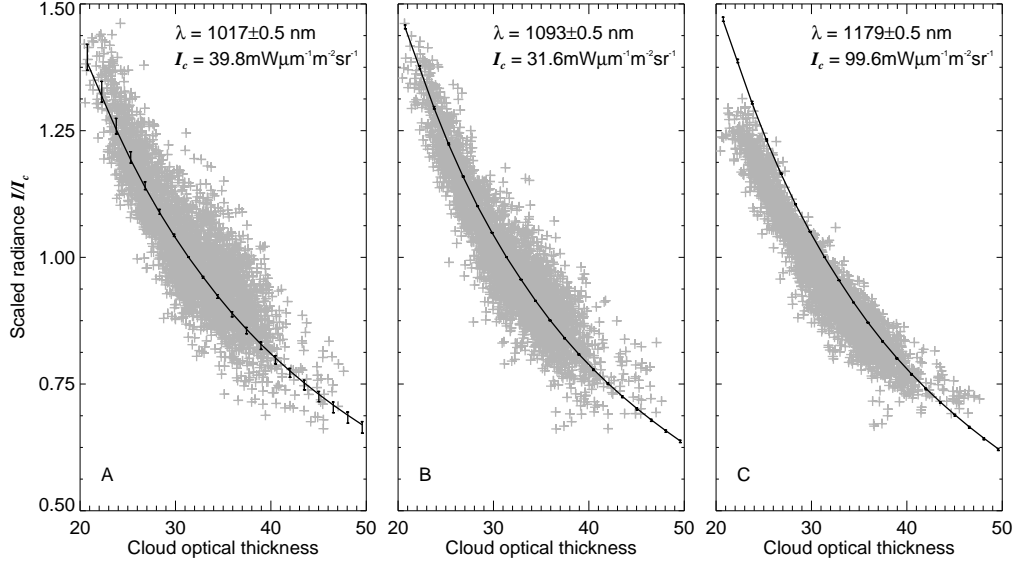


Figure 6: Scaled radiances and associated cloud opacities of a subset of the data and the model for the three windows at A) 1017 nm B) 1093 nm and C) 1179 nm. The data subset is a random sample of all data within the given wavelength interval and a small interval of topography and bandwidth. The model curve corresponds to the center of that interval while the error bars give model variation over the whole parameter space when scaled to unity at average cloud opacity.

Here band center wavelength has a more significant effect and we define the correction function by bi-linear interpolation between the synthetic radiances normalized to radiance at average bandwidth for each 1 nm wavelength interval of the parameter space.

Fig. 7 shows a sample of the data and correction function for a single 1 nm wavelength interval. The correction is in general small compared to data variance, and again the influence of other model parameters (topography from -1.5 km to 3.5 km, emissivity from 0.2 to 1, cloud opacity from 20 to 50) shown as error bars is negligible.

4.3. Topography and wavelength correction

4.3.1. Atmospheric blurring

The 1-D atmospheric radiative transfer model implicitly assumes that for each calculated case, i.e. each entry in the lookup table, the boundary geometry and conditions are constant and infinite horizontally, i.e. plane parallel. However in some locations the topography varies significantly over horizontal distances over which photons are scattered by the atmosphere. Monte-Carlo modeling shows that photons from a point source on the surface emerge from the top of the atmosphere with a density that can be described as a Gaussian of horizontal distance with a full width at half maximum of 90 km (Hashimoto and Imamura, 2001) to 100 km (Basilevsky et al., 2012).

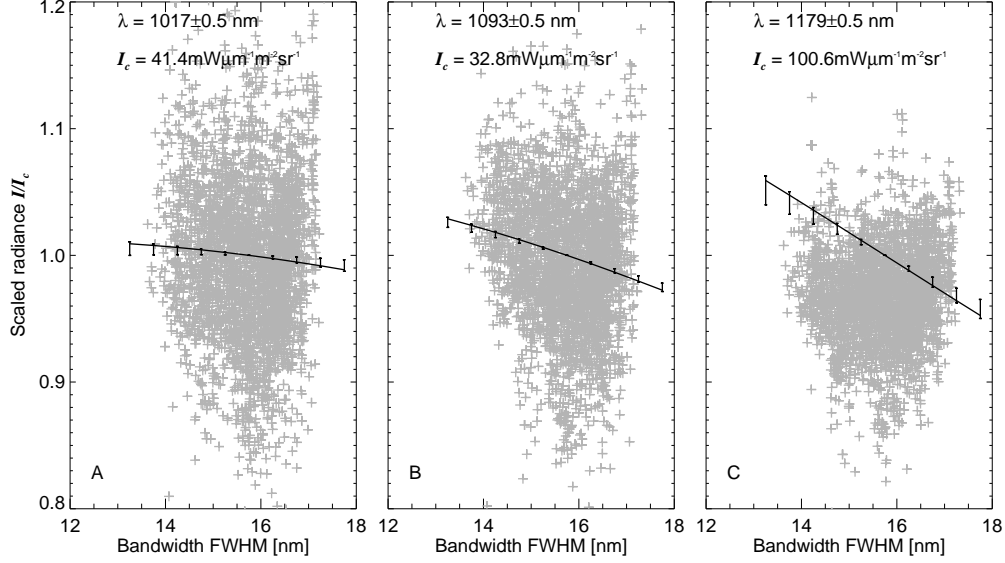


Figure 7: Scaled radiances and associated bandwidth of a subset of the data and the model for the three windows at A) 1017 nm B) 1093 nm and C) 1179 nm. The data subset is a random sample of all data within the given wavelength interval and a small interval of topography. The model curve corresponds to the center of that interval while the error bars give model variation over the whole parameter space when scaled to unity at average bandwidth.

To account for this horizontal scattering using a blurring method, we convolve the modeled top of atmosphere (TOA) radiances I_λ based on Magellan topography Z with a blurring function based on the Monte-Carlo modeling, similar to the approach of Mueller et al. (2008); Basilevsky et al. (2012) and Kappel et al. (2012, 2016). The blurring is performed for each VIRTIS spectrum to generate a specific look-up table for the location of its footprint. Also included in the calculation of the look-up table is the wavelength λ derived for each band of each VIRTIS spectrum.

In a preceding step we have corrected the data to the values it would have if the cloud opacity was constant at the average observed value and therefore we need to create the look-up table only for this constant opacity of 32.3. The remaining free parameter is emissivity e , so that the look-up table of convolved radiances is only a table of one dimension $I'_\lambda(e)$. The Magellan data cell size of 5 km is small compared to the blurring function and thus the convolved radiance can be represented by a weighted average of discrete values:

$$I'_\lambda(e) = \frac{\sum_i g(d_i) I_\lambda(Z_i, e)}{\sum_i g(d_i)} \quad (2)$$

where d_i is the great-circle distance between VIRTIS footprint and Magellan topography cell with index i , g is a Gaussian with a full width at half maximum of 90 km (Hashimoto and Imamura, 2001), and Z_i are the Magellan topography values in the vicinity.

There is a notable difference to the work of Basilevsky et al. (2012, Eq. 1 therein), who convolve only over

the blackbody radiance of the temperature corresponding to the topography instead of the top-of-atmosphere radiance derived from that. This neglects that the effects of scattering, absorption, and emission in the lower atmosphere that also appear blurred when observed from above the cloud layer.

While some of the atmospheric blurring occurs in the layer below the highest topography (12 km), the cloud layer between 50 and 70 km altitude is responsible for most of it. The blurring function full width at half maximum is approximately two times the altitude of the scattering layer (Moroz, 2002). Therefore we think that the blurring of TOA radiances, our eq. 2, is more accurate than the blurring of surface radiances, i.e. eq. 1 in the work of Basilevsky et al. (2012).

In the following we will show data and models in relation to surface topography. Since there is no single topography value that can be associated with each radiance value, we calculate for each spectrum and each band the topography value that would correspond to the modeled radiance in a plane parallel atmosphere by inverting the radiance function $I_\lambda(Z, e)$ at the emissivity $e=0.8$ that we will use to estimate continuum opacity in the next section:

$$Z_\lambda = I_\lambda^{-1}(I'_\lambda)|_{e=0.8} \quad (3)$$

The resulting sets of blurred topography values are specific for each window observed by VIRTIS. In the following we will use the subscript of Z_λ only to identify the window, but note that the variable band center wavelengths have been used in the calculations.

The differences between the three topography sets ($Z_{1.02\mu m}$, $Z_{1.10\mu m}$, $Z_{1.18\mu m}$) are rather small, less than 25 m in the areas we studied here. This indicates that the functions I_λ , though very different in relative gradient with respect to topography (see Fig.8), are fairly linear functions relative to topographic variance within each blurring radius. This also confirms the statements from Mueller et al. (2008) and Kappel et al. (2012) that the details of the calculation of a blurred topography calculated along the lines of Eq. 2 and Eq. 3 are not really significant for the final result. Many previous studies (Helbert et al., 2008; Mueller et al., 2008; Mueller et al., 2012; Mueller et al., 2017; Smrekar et al., 2010; Kappel et al., 2012, 2016; Gilmore et al., 2015; Stofan et al., 2016; D’Incecco et al., 2017) relied on a blurred topography with some approximate $I_\lambda(Z)$. This blurred topography was then used to model TOA radiance, either statistically or numerically. We have confirmed that this use of a blurred topography does not result in significantly different results from this approach, which integrates the blurring into the inversion to emissivity. The above mentioned previous studies are therefore still valid and, aside from differences in the radiance model, comparable with our results. This applies to the work of Kappel et al. (2016) even though they use topography blurred appropriate for the 1.02 μm window (Kappel et al., 2012) for the 1.10 μm and 1.18 μm windows.

4.3.2. Continuum absorption

There is an ambiguity between the unknown CIA and the unknown surface emissivity. To move forward we assume an average surface emissivity and fit the CIA coefficient by minimizing the χ^2 between the model

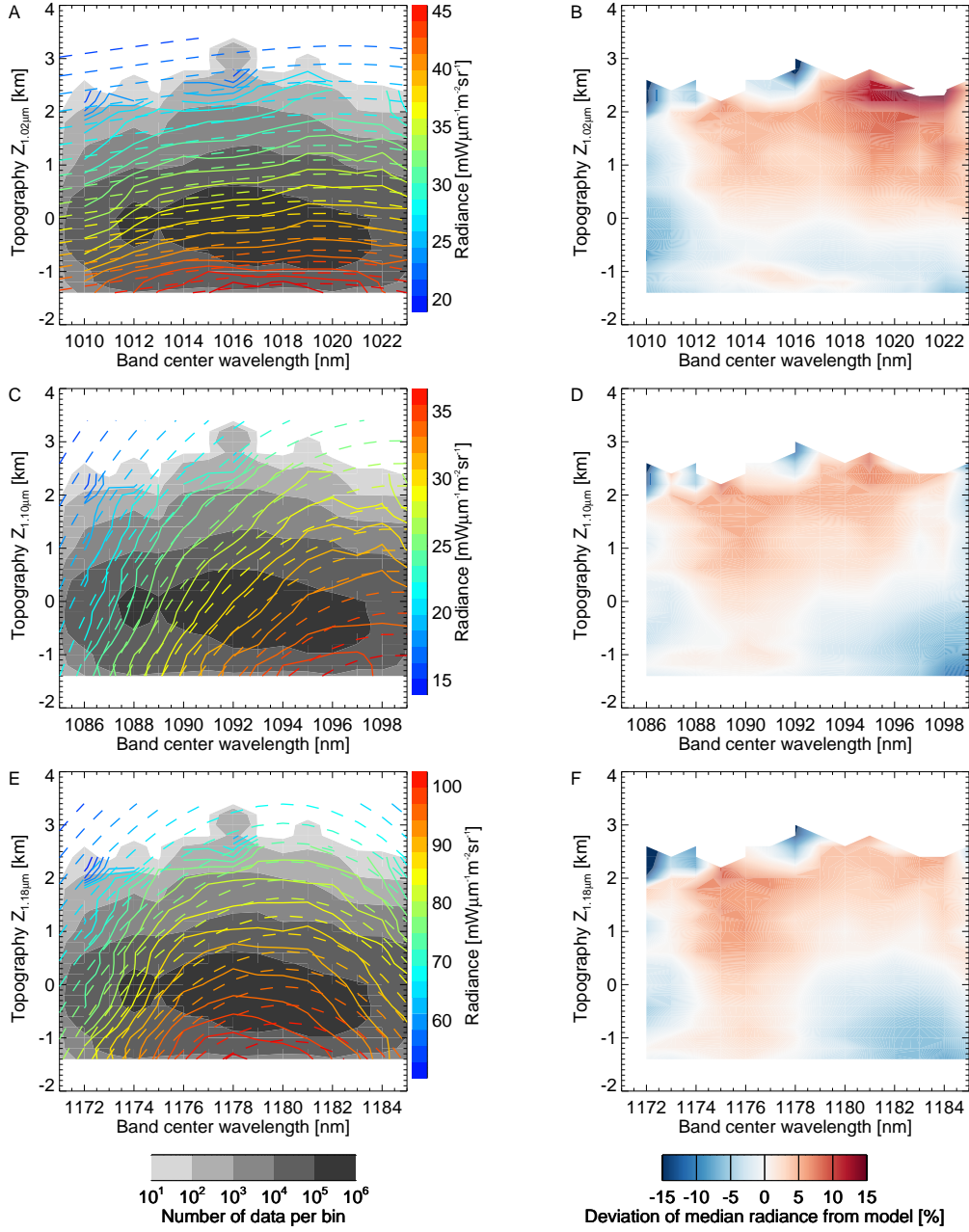


Figure 8: Left column: Grayscale shows number of data per 1 nm x 200 m bin. Solid contours show cloud and bandwidth corrected radiances median of each bin, broken contours show the model radiances fitted to the data using the CIA as fitting parameter. Right column: Color scale shows the deviation of model from median data.

and the data corrected for limb darkening, cloud opacity, and bandwidth.

Fig. 8 shows the average of radiance binned on a wavelength and blurred topography grid and the fitted model radiance, and their deviations from each other. The fit in Fig. 8 assumes an emissivity of 0.8, which is best fitted by a CIA of 0.20×10^{-9} , 1.17×10^{-9} , and $0.99 \times 10^{-9} \text{ cm}^{-1} \text{ amagat}^{-2}$ for the 1.02, 1.10 and 1.18 μm window, respectively.

We have ascertained that the details of the atmospheric blurring do not affect this fit. In an initial step we used the $I_\lambda(Z)$ derived from statistics of the 1.02 μm radiances (Mueller et al., 2012) to generate a blurred topography as described in the previous section. This is used to find the best fitting CIA coefficients for each of the three windows. These CIA coefficients are used in the calculation of the band specific blurred topography sets ($Z_{1.02\mu\text{m}}$, $Z_{1.10\mu\text{m}}$, and $Z_{1.18\mu\text{m}}$) which are then used to fit the CIA coefficients again, but the same values are obtained in this second iteration.

The deviation between average data and model shows a similar pattern in all three windows, with a trend towards lower than modeled radiances at very short wavelengths and higher radiances and long wavelengths. There is a consistent trend with topography in all windows. The deviation with respect to wavelength might be indicative of a problem in modeling the spectral shape of the 1.31 μm window (Fig. 5), or possibly a change of the instrumental straylight with instrumental temperature or position on the detector. The deviation with respect to topography is equivalent to a trend of derived emissivity with topography, a problem similarly encountered by most models of surface thermal emission that assume the VIRA temperature profile (Seiff et al., 1985), namely the works of Meadows and Crisp (1996); Hashimoto et al. (2008); Haus and Arnold (2010); Basilevsky et al. (2012); Kappel et al. (2016).

The systematic deviation of model and data as a function of topography is affected by the choice of assumed surface emissivity, but the trend would only disappear at unphysical emissivities greater 1, if at all. The trend is equivalent to the model overestimating radiances below 0 km elevation and thus indicates missing opacity, if interpreted in terms of atmospheric absorption. An assumption of a lower emissivity however requires only a smaller CIA to match average absolute radiance (see Fig. 9) and thus only increases the trend.

Bézar et al. (2009) use VIRTIS data and Bézar et al. (2011) use SPICAV data (Korablev et al., 2012) to find the CIA that matches the relative trend of observed radiance and topography. They also assume a uniform surface emissivity but allow for a free constant factor to the spectra with the argument that cloud opacity is not well known and spectrally flat. Fedorova et al. (2015) use the ratio of window peak radiances at 1.10 and 1.185 μm to the radiance of an airglow free part of the 1.27 μm to constrain continuum opacity, because this ratio is relatively insensitive to cloud opacity. They however still fit only the gradient with respect to topography and not the absolute value to reduce the impact of calibration uncertainties. Fedorova et al. (2015) find an increase of the best fit CIA with decreasing surface emissivity when fitting SPICAV topography range of -1 to +1 km.

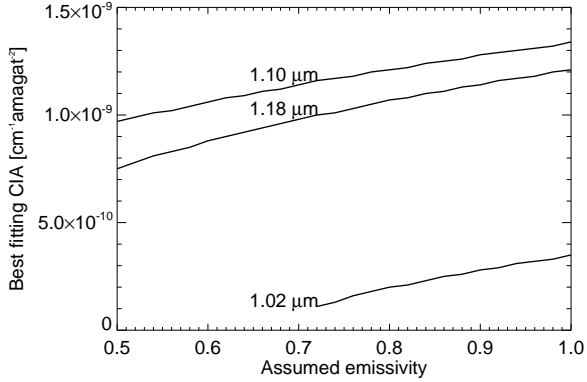


Figure 9: The fitted CIA coefficients as function of the assumed emissivity. We did not model CIA less than $1 \times 10^{-10} \text{ cm}^{-1} \text{ amagat}^{-2}$.

The CIA coefficients relying only on the relative gradient with topography (Bézard et al., 2009, 2011; Fedorova et al., 2015) are generally slightly smaller than our values at an emissivity of 0.95 and in the range of 0.4 to $1 \times 10^{-9} \text{ cm}^{-1} \text{ amagat}^{-2}$ for the 1.10 and $1.18 \mu\text{m}$ windows. This is consistent with laboratory measurements at room temperature and at near Venus surface pressure of $0.5 \times 10^{-9} \text{ cm}^{-1} \text{ amagat}^{-2}$ (Snels et al., 2014b).

Our slightly larger CIA coefficients fitted to absolute radiance might indicate other opacity missing from the model, e.g. sub cloud aerosols (Sagan, 1975; Satoh et al., 2009). On the other hand, the effect of temperature on CIA is not well understood (Snels et al., 2014a) and the room temperature laboratory data might underestimate the continuum. The estimates based on gradient only (Bézard et al., 2009, 2011; Fedorova et al., 2015) all rely on the atmospheric temperature profile of the VIRA model (Seiff et al., 1985), which for altitudes $< 6 \text{ km}$ has high uncertainties (Lebonnois and Schubert, 2017) and deviates significantly from the most recent in-situ data of VeGa 2 (Seiff, 1987).

4.3.3. Inversion to emissivity

To invert the VIRTIS radiances to surface emissivity we use the specific lookup table for each spectrum described in section 4.3.1, which is based on the topography in the vicinity of the footprint and the specific band center wavelength of each observation. The lookup tables are calculated using the CIA coefficients best fitting all the data assuming an emissivity of 0.8, derived in the previous section. This means that the inverted emissivity is calibrated to be on average of 0.8. We invert the data by interpolating between lookup table radiances to find the emissivity e where data and model are equal. In case of data out of the modeled range ($0.2 < e < 1$) we extrapolate linearly.

The VIRTIS image cubes that have been reduced to 3 bands of emissivity are then projected onto a

common grid defined by Lambert’s azimuthal equal area projection centered on the south pole, and then combined to a mosaic by taking the median emissivity of each grid point. The map is constructed from more than 1000 image cubes, covering the same location at up to 200 different times. The three band maps are shown in Fig. 10.

5. Results

5.1. Southern Hemisphere Emissivity Maps

The emissivity maps show a correlation to topography that is visualized in the scatterplots of Fig. 10. The trend of derived emissivity in relation to topography is similar in all three bands. At the higher range of topographies sampled by VIRTIS, about 1000 to 3000 m above 6051 km radius the correlation is small, but increases towards the lowlands.

The amplitude, i.e. the maximum deviation from emissivity 0.8 to which the CIA coefficients are fitted, is different in the three windows. This is a result of the varying sensitivity of derived emissivity to observed radiance owing to the varying atmospheric transparency. Fig. 8 shows that the relative deviations between average radiance and model are of a similar magnitude in each of the three windows.

Such trends in emissivity derived with atmospheric radiative transfer models have been previously reported by (Meadows and Crisp, 1996; Basilevsky et al., 2012; Kappel et al., 2016). There are several possible causes, incorrect temperature in the model, missing opacity in the model, e.g. from dust or haze, or an actual link between emissivity and topography such as observed at centimeter wavelengths (Pettengill et al., 1991; Klose et al., 1992).

A so far unreported observation is that the trend varies from region to region. The regions described in the following are in the same latitude band and in the range of longitudes covered by many VIRTIS observations (see Mueller et al., 2008), which reduces instrumental and atmospheric noise. The emissivity trend in Themis Regio (blue in Fig. 10) is steeper than in the region including Lavinia Planitia (red in Fig. 10). At the lowest elevation in the Themis region of about 800 m, the difference in emissivity to the same elevation in Lavinia Planitia is about 0.07 at 1020 nm wavelength. This corresponds to a difference in surface brightness temperature of about 4 K.

This difference in brightness temperature can be used as rough estimate if attributed to a deviation of surface temperature from the model assumption of it following the vertical profile of the VIRA model Seiff et al. (1985). This is less useful for the 1100 and 1180 nm windows, where more of the observed emission originates from the atmosphere and thus depends significantly on the whole vertical profile.

There are differences in the local time of observations in different regions, but diurnal temperature variation does not seem to be a straightforward explanation for the deviations. The average of local time

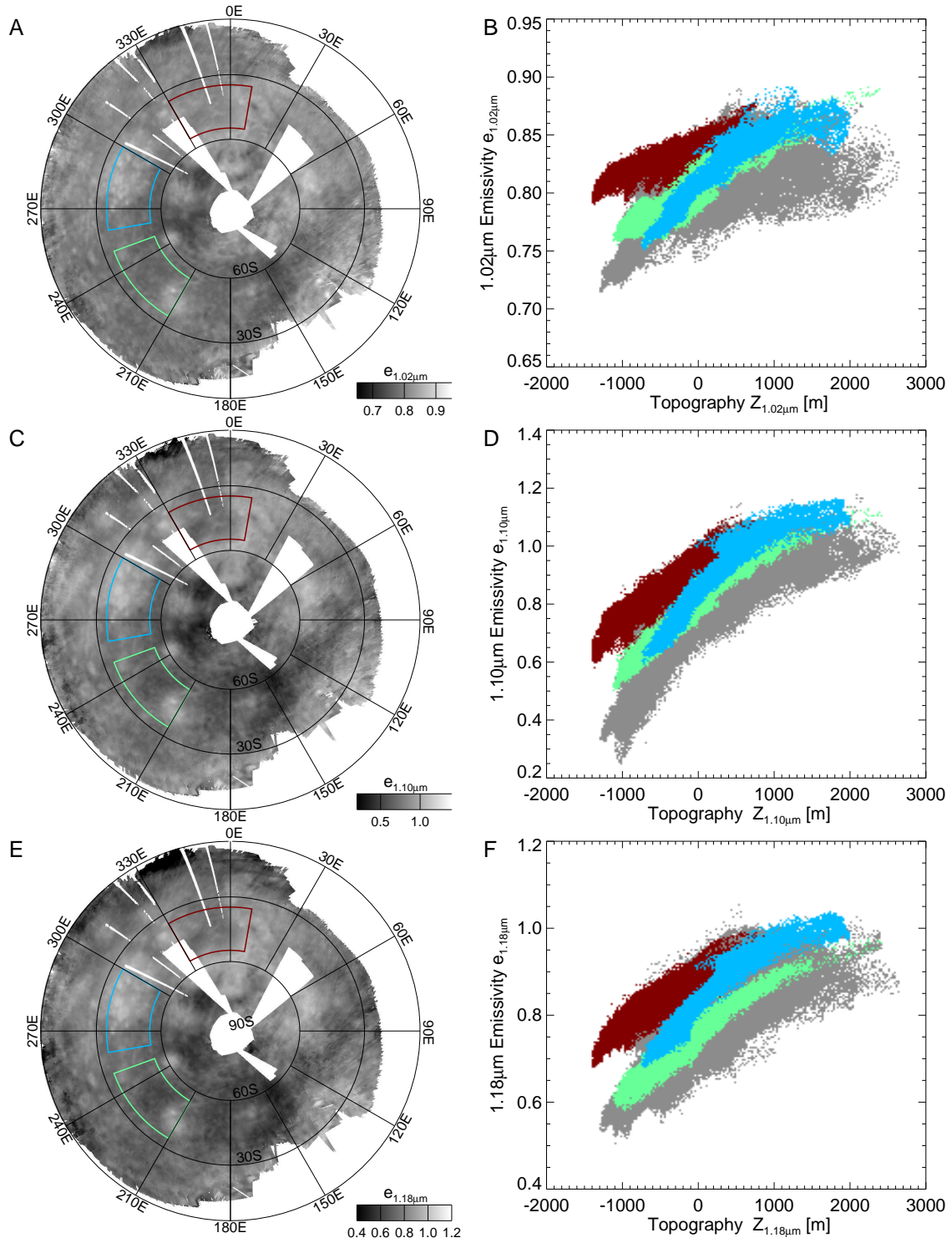


Figure 10: Maps of emissivity at A) 1020 nm, C) 1100 nm, and E) 1180 nm. Scatterplots of emissivity at B) 1020 nm, D) 1100 nm, F) 1180 nm versus topography overall (grey symbols) and in selected regions in (colored symbols). Red indicates Lavinia Planitia, blue Themis Regio, and green Imdr Regio. 19

of observations is 5 to 7 hours after sunset in Themis and 7 to 9 hours after sunset in Lavinia, yet Lavinia shows higher thermal emission contrary to the expected cooling during the night hours.

5.2. Local emissivity trends

Kappel et al. (2015, 2016) make the argument that the lower atmosphere temperature has a large lateral correlation length on the order of thousands of kilometer based on Venus General Circulation Model (GCM) results (Lebonnois et al., 2010), in other words that the lateral temperature gradients are small. This is in line with the theoretical discussion of Stone (1975) that timescales of convective heat transport are much shorter than that of radiative heating and cooling, so that any locally increased solar heating would be efficiently redistributed.

Assuming that the systematic trend with topography is caused by a deviation of the temperature profile from our assumed profile with small lateral gradients, it is appropriate to characterize the trend observed in the data and to interpret the local variations relative to this trend. This is similar to the work Kappel et al. (2016) renormalization of emissivity maps after removing a linear trend of emissivity with topography.

For this we select subregions that are likely composed of basalt, i.e. volcanic plains and flow fields, and we stay away from regions with steep slopes such as tessera, rifts and ridge belts, which are not well resolved by the Magellan altimetry. In the following we show for two regions, Themis Regio and Lavinia Planitia, that the trend in different subregions is consistent so that the emissivity over that entire region can be interpreted relative to the trend, taking into account the variance relative to the trend as measure of uncertainty. Themis Regio was frequently observed by VIRTIS on Venus Express and is relatively well studied in the near-infrared (Mueller et al., 2008; Smrekar et al., 2010; Stofan et al., 2016; Kappel et al., 2016).and its emissivity trend is close to the global average. Lavinia Planitia has the largest deviation from the global average trend (Fig. 10). Each location in the two areas studied here is covered by approximately 100 to 150 different VIRTIS images, with coverage decreasing towards North.

5.2.1. Themis Regio

The regions that we select to represent the emissivity trend are outlined in Fig.11. Region a) is the whole region for context and is not used in the derivation of the emissivity trend, since it includes significant real variation of emissivity and rifts (Parga Chasma) that might not be resolved well in Magellan altimetry. Region b) is composed mostly of plains with wrinkle ridges, but it also includes a crater with a bright ejecta parabola (Abington). Region c) is composed of smooth plains associated with Darclee Patera and Zemaite Patera. Region d) is on the north-western flank of Shiwanokia Corona and covered by a dark ejecta parabola from crater Sabin. Region e) encompasses lava flows on the eastern flank of Shiwanokia Corona. Region f) encompasses flows on the south-eastern Flank and some interior of Shulamite Corona.

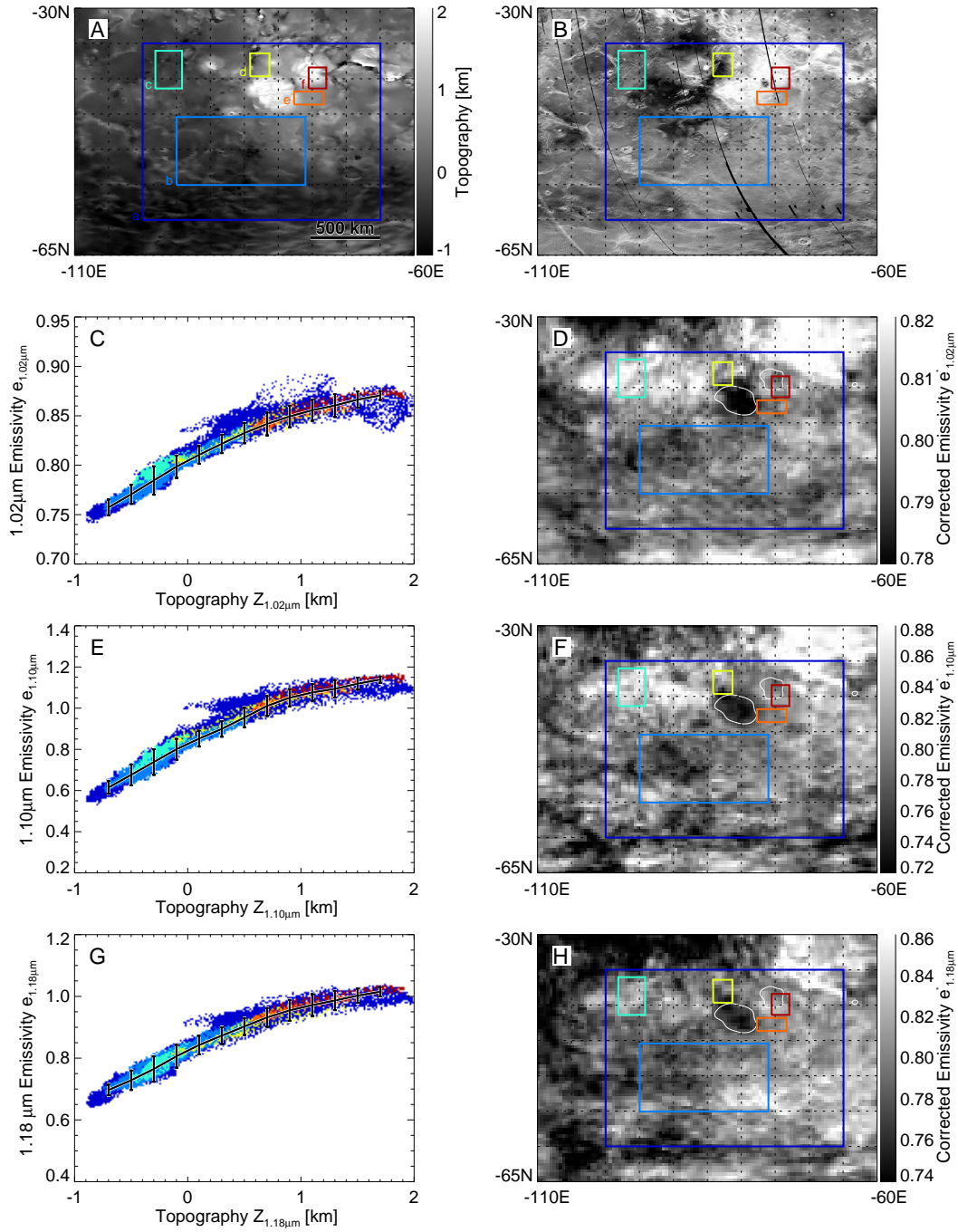


Figure 11: A) Magellan altimetry and boxes outlining selected subregions of Themis Regio. B) Magellan synthetic aperture radar image. Derived emissivity vs topography, and trend derived from subregions for C) 1020 nm, E) 1100 nm, and G) 1180 nm. Emissivity maps corrected for the trend shown in the right column for D) 1020 nm, F) 1100 nm, and H) 1180 nm. White outline in the emissivity plots indicates 1500 m above MPR in the altimetry degraded to infrared resolution.

We calculate the average emissivity and its standard deviation in 200 m elevation bins for regions b) to f) and define the emissivity trend as a function of specific blurred topography $e'(Z_\lambda)$ via interpolation between the points given by the average of topography and emissivity in each bin. The trend of 1.02 μm emissivity is roughly consistent with the trend of emissivity derived by Kappel et al. (2016), which is described with an average slope of 2 - 5% per km, depending on selection of measurements and atmospheric parameter assumption (Kappel et al., 2016, Fig. 2, Table. 4), consistent with our trend of 10% over 2.5 km.

We find qualitatively similar but higher amplitude trends in the 1.10 and 1.18 μm emissivities, unlike the retrievals of (Kappel et al., 2016), which show trend with a negative sign at 1.10 μm and a generally small trend at 1.18 μm . We note that in case of an incorrect temperature profile and otherwise correct parameters used in the atmospheric radiative transfer model, the resulting emissivity trend can be expected to be qualitatively similar in the three windows.

Regardless of what causes the trend, it is possible to correct for it as long as it is locally consistent. The subregions that we selected all follow the trend (Fig. 11), although there may be some systematic deviations. These could be related to systematic trends of atmospheric parameters with latitude, or residual calibration errors or straylight. In any case the systematic deviations are not large compared to the 2σ variances of the bins so we can confirm the trend to be consistent over Themis Regio.

We correct the emissivity maps by dividing by the values of the function $e'(Z_\lambda)$ interpolated to the appropriate altimetry and multiplication with 0.8, the average emissivity that is consistent with the chosen continuum opacity. We take the largest standard deviation of any of the elevation bins $e'(Z_\lambda)$ as a measure of uncertainty σ . This uncertainty provides a likelihood for the emissivity of a single mapping tile of approximately $20 \times 20 \text{ km}^2$ to fall within a certain distance of the trend. The likelihood that the average of a number of tiles corresponding to a geological feature exceeds the uncertainty by chance is lower, but this cannot be directly estimated from the standard error on the mean because the errors are spatially correlated. Still we content that a group of tiles associated with a geological feature with diameters on the order of hundreds of kilometers deviating on average from the trend by 1σ or more is very likely a significant anomaly.

The corrected emissivity maps in a gray scale stretched to represent the 2σ error are shown in Fig. 11. For the 1020 nm band this is approximately the same as the 2% deviation from the average that was used by Stofan et al. (2016) to define significant emissivity anomalies.

The corrected 1020 nm map is similar to that presented by Stofan et al. (2016) and Kappel et al. (2016). Table 1 lists features discussed in the work of Stofan et al. (2016) with coordinates and values of emissivity extrema associated with them. As in the maps interpreted by Stofan et al. (2016) the correlation between geologic features is not perfect but the general location of unusual emissivity remains the similar with some exceptions. The low emissivity anomaly at the top of Shiwanokia Corona, which had also been observed by Kappel et al. (2016), now appears larger. The high emissivity anomaly that previously encompassed the

Feature name	Lon [deg]	Lat [deg]	Emissivity	Notes
High emissivity reported in the work of Stofan et al. (2016)				
Abeona Mons	-86.78	-44.78	0.809	
Chloris Mons	-65.47	-45.47	0.809	
Mertseger Mons	-89.69	-38.16	0.812	
Mielikki Mons	-89.70	-27.8	–	outside of this study area
Semiramus Corona	-67.28	-37.13	0.818	regionally increased emissivity
Zywie Corona	-68.88	-38.78	0.812	near Parga Chasma
Latta Corona	-72.38	-37.91	0.813	near Parga Chasma
Shulamite Corona	-76.84	-38.16	0.809	anomaly on north-western rim
Ukemochi Corona	-64.03	-40.25	0.807	near Parga Chasma
Shiwanokia Corona	-84.31	-41.56	0.807	anomaly on western flank
Nzambi Corona	-71.19	-45.19	0.811	anomaly on flank flows
Bibi Patma Corona	-58	-47	–	outside of this study area
Low emissivity reported in the work of Stofan et al. (2016)				
Ukemochi Corona	-64.78	-38.88	0.788	dark plains in interior
Shiwanokia Corona	-80.59	-42.09	0.768	interior
unnamed volcanic center material	-65.88	-41.84	0.791	

Table 1: Volcanoes and coronae reported to have anomalous 1020 nm emissivity in the work [Stofan et al. \(2016\)](#) and the coordinates and values of extrema associated with these features in our work.

north-western flank of Shiwanokia corona at elevations higher than our reference region d) is reduced to a smaller area in the west.

The observation of low emissivity at the top of Shiwanokia corona has to be understood relative to the top of Shulamite Corona, the only region with comparable surface elevation. The corrected emissivity maps include a 1500 m topography contour to mark regions that rely only on one reference region for correction and are thus more susceptible to correlation of true emissivity with topography. The 1100 and 1180 nm maps have uncertainties of 10 and 6%, respectively and do not show clear anomalies exceeding this threshold except at Parga Chasma, which is likely an artifact of unresolved topography. Parga Chasma is associated with steep rifts approximately along the line from -30N,-85E to -40N,-60E. In addition to these possibly not fully resolved rifts, the region north of Parga Chasma seems to be affected by a diffuse increase in emissivity that does not correlate to identifiable features.

5.2.2. Lavinia Planitia

For comparison we investigate the local trend at Lavinia Planitia over the same latitude range. Within the region well covered by VIRTIS this shows the largest deviation from the Themis Regio trend (Fig. 10). Lavinia Planitia is a basin with the topographic minimum approximately 1500 m below the 6051.840 km median planetary radius (MPR) (Ford and Pettengill, 1992). It is bounded on the East by higher terrain in form of a rift connecting a series of coronae reaching elevations up to 1000 m above MPR (Baer et al., 1994; Magee and Head, 1995) and to the south by a rift zone (Kalaipahoa Linea) and associated ridge on the northern flank of 3 km high Lada Terra (Magee and Head, 1995; Ivanov and Head, 2006). To the north-west gentler slopes lead up to the highland of Dione Regio. The surrounding rifts are the apparent source for several huge, stratigraphically young lava flow fields (Eriu, Kaiwan, Mylitta Fluctūs) extending down into Lavinia Planitia covering $>10^5$ km² and an elevation range >2 km (Magee Roberts et al., 1992; Magee and Head, 1995). Early analysis of VIRTIS data (Helbert et al., 2008) showed an apparent increase in emissivity at Mylitta Fluctus but this can be attributed to the local trend of Lavinia Planitia, which is equivalent to higher emissivities compared to the global average trend used for the data reduction in the work of (Helbert et al., 2008).

The interior of Lavinia Planitia shows belts of tectonically deformed terrain with positive relief (Hypolyta, Antiope, Molpadia, Penardum Lineae), that are mapped as stratigraphically older than the adjoining regional plains with wrinkle ridges (Ivanov and Head, 2001, 2006). Because terrain with tectonic deformation has less reliable altimetry, we select subregions in plains with little topographic relief, shown in Fig. 12. Region a) is for larger scale context and encompasses the part of Lavinia Planitia with the globally unusual trend. Region b) follows Mylitta Fluctus on the northern slope of Lada Terra, Region c) follows parts of Kaiwan Fluctus on the south western slope of Selu Corona, Region d) is encompasses mostly plains without clear lava flow features but some lineations and wrinkle ridges (Ivanov and Head, 2001; Bridges and McGill, 2002) on the western flank of Selu Corona, and region e) is mostly also composed of plains with wrinkle ridges on the south facing slope of Dione Regio.

Overall, region a) is consistent with the local trend derived from region b) - e) (Fig. 12), there are few outliers. In regions b) to e) there is no clear evidence that position in the local stratigraphic sequence or direction of slope have an impact on the trend. There is no evidence that coincidental correlation of surface composition or texture with elevation affects the trend, the subregions are geologically relatively uniform.

The largest variance within the topography bins translates to a 2σ of 1.5%, 10% and 4% for the 1020, 1100 and 1180 nm windows. The emissivity relative to this trend (Fig. 12) shows few deviations outside of 2σ around the average. The largest deviations occurs at the southern and eastern rim of Lavinia, which might be artifacts because rifts and associated steep slopes are not well resolved by Magellan altimetry, because there is little VIRTIS data of that elevation range to define the trend, and because this seems to be

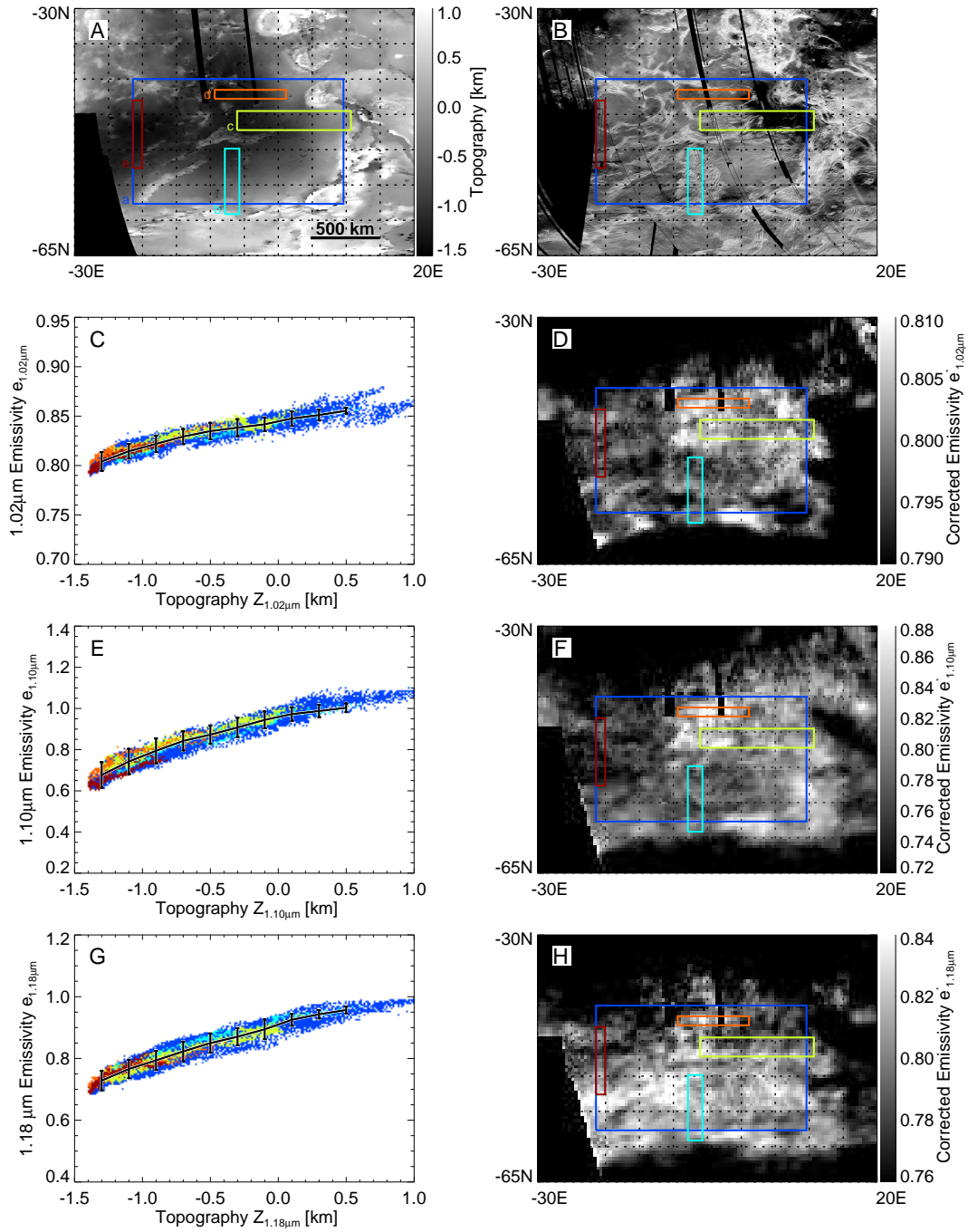


Figure 12: A) Magellan altimetry and boxes outlining selected subregions of Lavinia Planitia. B) Magellan synthetic aperture radar image. Derived emissivity vs topography, and trend derived from subregions for C) 1020 nm, E) 1100 nm, and G) 1180 nm. Emissivity maps corrected for the trend shown in the right column for D) 1020 nm, F) 1100 nm, and H) 1180 nm.

a boundary of the region where the emissivity trend is internally consistent.

5.3. Theoretical emissivity uncertainty in comparison to observed variance

[Kappel et al. \(2015\)](#) provide a very detailed and insightful study of the uncertainty of emissivity derived from fitting the observed radiance with a radiative transfer model given the uncertainty of atmospheric parameters. The part dealing with uncertainties resulting from the use of cloud opacity derived only from the 1310 nm window ([Kappel et al., 2015](#), Sect. 4.2) is highly applicable to this study, and paraphrased here in the following.

They distinguish broadly between three kinds of errors arising from the uncertainty of atmospheric parameters, errors varying (1) in time and space, (2) only in space, (3) neither space nor time. The different atmospheric parameters contributing to the first kind of error with the assumed 2σ uncertainties in brackets are the following: the relative abundance of cloud particle size modes (50%), the altitudes at which the different cloud particle modes occur (3 km), the H_2SO_4 concentration of cloud droplets (7.5%), H_2O column (25%). These errors together are called *atmospheric noise* in the following. The errors of the second kind are the surface elevation (200m), surface temperature (3K), temperature at 25 km altitude (3K). Errors of the third kind are the deep atmosphere continuum absorption in the four windows (25%).

For a single spectrum the absolute emissivity errors from these uncertainties are large, in the three surface windows the atmospheric noise is given as 14, 76, and 78%, for the 1020, 1100 and 1180 nm bands, respectively. The spatially varying emissivity errors are given as 35, 65 and 65 % and the continuum errors are 32, 108 and 93 %. [Kappel et al. \(2015\)](#) also provide an estimate of the uncertainty due to VIRTIS instrumental noise modeled as normally distributed random variable with a standard deviation of $0.0001 \text{ W}\mu\text{m}^{-1}\text{m}^{-2}\text{sr}^{-1}$, resulting in 7, 24 and 23 % errors.

We find that these calculations are consistent with our observations. Instrumental and atmospheric noise can effectively be reduced by averaging over many observations. In the areas studied here, i.e. Themis Regio and Lavinia Planitia, we average over approximately 100 images, equivalent to an order of magnitude smaller error on the mean. The errors varying only spatially cannot be reduced by averaging but the numbers of [Kappel et al. \(2015\)](#) for a single spectrum likely provide an overestimate of this error. [Kappel et al. \(2015\)](#) discuss that the near surface atmospheric temperature including the 25 km altitude source region of the 1310 nm window can be expected to be correlated over distances of 10^3 km. The relative errors given by [Kappel et al. \(2015\)](#) for retrieval errors from multiple spectra using a statistical model including the correlation lengths and times of atmospheric parameters ([Kappel, 2014](#)) of less than 2% are likely more appropriate. The cited 2σ error of the Magellan altimetry of 200 m is likely not representative of data in smooth plains that we use to construct the local trends and errors are furthermore statistically reduced by the averaging over many radar footprints in simulation of the blurring effect of the atmosphere ([Hashimoto and Imamura, 2001](#); [Mueller et al., 2008](#)).

The difference between our local trends is well within the errors for surface and atmosphere temperature uncertainty of 3 K, and we can confirm that this kind of spatial error is consistent over the regions we studied. Relative to the local trends we typically find root mean square deviations of 1, 5 and 3 % for the 1020, 1100, and 1180 nm windows. This is roughly consistent with the statistically reduced combined atmospheric and instrumental noise modeled by (Kappel et al., 2015), in addition to some emissivity variation and spatially slowly varying surface temperature variation.

Not much can be done or learned about the continuum errors, but this only affects the absolute emissivity, not local variation. The average absolute emissivity of Venus consistent with this work is between 0.6 and 1 at 1020 nm, and mostly unconstrained in the other windows, consistent with the 100 % continuum error calculated by Kappel et al. (2015).

5.4. Emissivity Spectra

While the absolute emissivity is very uncertain, its relative variation shows some significant deviations from the regional background in Themis Regio. In order to use these data to constrain surface composition, it is necessary to assume a spectrum for the background. An appropriate spectrum for this is basalt, chemically weathered under Venus conditions and measured at Venus temperatures. High temperature laboratory measurements are important as emissivity and spectral slope of basalt and some expected weathering products have been observed to change significantly (e.g. Pieters et al., 1986; Yamanoi et al., 2009). There is on-going work to create a library of such spectra (Helbert et al., 2017). To some extent it is possible to constrain that background spectrum using the in-situ reflectance measurements by Venera-9 as one of those very broad band filters overlaps with the 1020 nm window (Ekonomov et al., 1980).

Fig. 13 shows average, locally corrected emissivity in the form of a false color map of Themis Regio and average spectra of selected regions. The local correction assigns a spectrally constant emissivity of 0.8 to the average of the sample regions, but this could be replaced with an appropriate spectrum of weathered basalt in future work. The three channels of the false color map are stretched to represent the range of $0.8 \pm 2\sigma$ for each of the three bands, red for 1020 nm, green for 1100 nm, and blue for 1180 nm. An area with a 2σ reliable emissivity anomaly would therefore show up as fully saturated or unsaturated in the corresponding hue. The 1020 nm anomalies are the most significant and thus the most prominent bright features in the false color map appear reddish.

The hue varies somewhat between these features, but this is not necessary a significant variation of spectral shape. To investigate further we outline 5 example areas and plot the average spectra in Fig 13D. The areas are Abeona Mons, a shield volcano with a steep sided dome at the top, an unnamed volcanic edifice centered at $-81^\circ\text{E}, -37.5^\circ\text{N}$ and its surrounding patch of more pronounced fractures, the inner bright ejecta paraboloid of crater Sabin at $-85^\circ\text{E}, -38^\circ\text{N}$ (Campbell et al., 1992), and the interiors of the coronae Shiwanokia ($-42^\circ\text{N}, -81^\circ\text{E}$) and Shulamite ($-38.8^\circ\text{N}, -75.3^\circ\text{E}$).

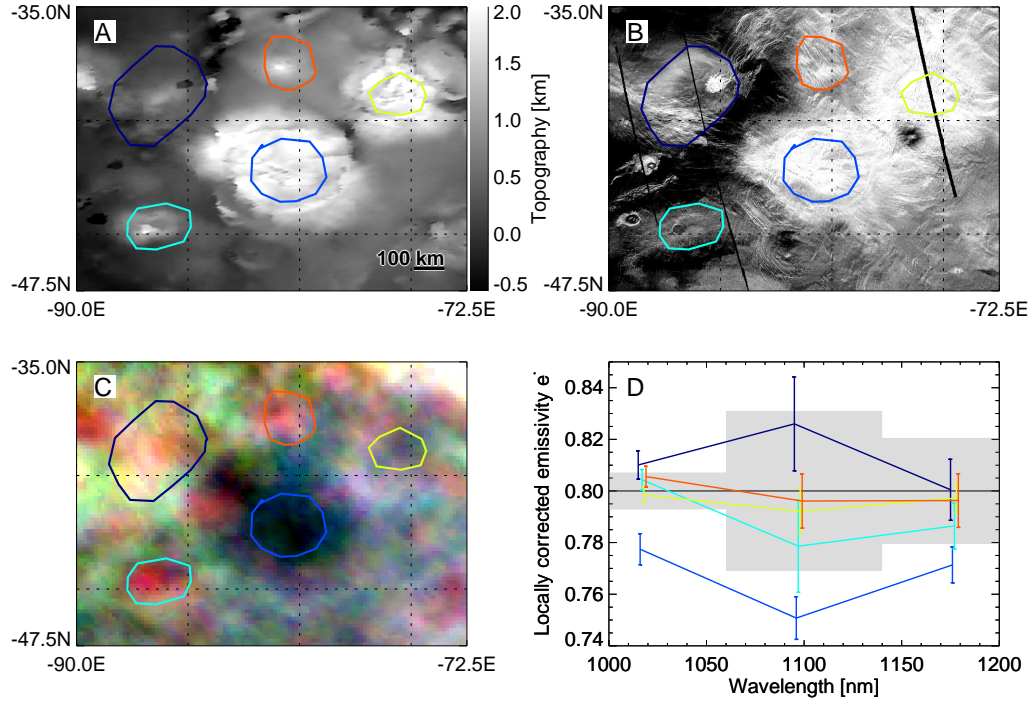


Figure 13: A) Magellan altimetry and outlines of selected subregions of Themis Regio. B) Magellan synthetic aperture radar image. C) false color image using the locally corrected emissivity maps stretched to $\pm 2\sigma$ of the local trend with red: 1020 nm, green: 1100 nm, blue: 1180 nm. D) average locally corrected emissivity spectrum of each of the subregions with error bars indicating the standard deviation. Purple: crater Sabin and innermost part of ejecta paraboloid. Blue: top of Shiwanokia Corona. Teal: Abeona Mons. Yellow Top of Shulamite Corona. Orange: unnamed volcano north of Shiwanokia. Solid black line and grey area illustrate the reference emissivity $0.8 \pm 1\sigma$ for each band.

The crater might be relatively young since its inner bright ejecta paraboloid is well preserved and the false color map suggests that there could be a difference in spectral shape between the volcanos and the crater ejecta. In addition to a 1σ anomaly in the 1020 nm band comparable to those of the volcanos, the 1100 nm emissivity of the ejecta is also high, though not exceeding 1σ . The single band map (Fig. 11F) shows that this increased 1100 nm emissivity is not as clearly correlated with the bright inner ejecta as the 1020 nm band but instead part of a more diffuse anomalous region extending westwards from the crater to -100°E . This therefore is not likely a real anomaly since it does not correlate well with geology or the 1020 nm band.

The deviations of the 1100 nm and the 1180 nm bands from 0.8 are all less than 1σ and do not clearly correlate with the 1020 nm band, with exception of the interior of Shiwanokia corona. The interior of Shiwanokia corona has lower emissivity in all bands than the interior of Shulamite corona, which has a similar surface elevation. The low emissivity of Shiwanokia Corona (Stofan et al., 2016; Kappel et al., 2016)

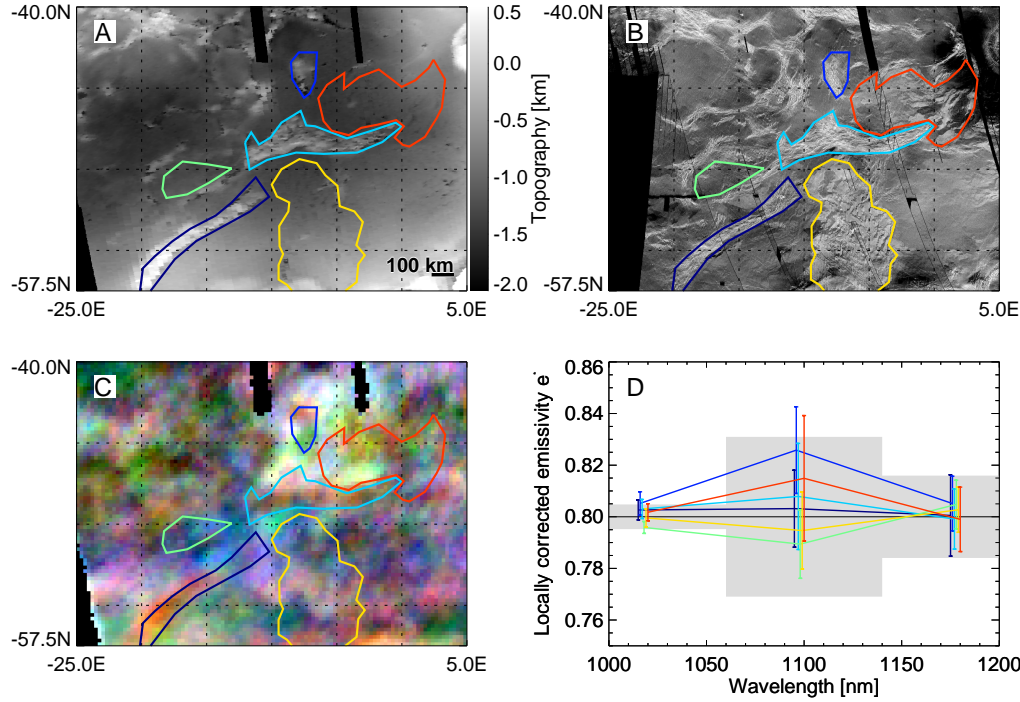


Figure 14: A) Magellan altimetry and outlines of selected subregions of Lavinia Planitia. B) Magellan synthetic aperture radar image. C) false color image using the locally corrected emissivity maps stretched to $\pm 2\sigma$ of the local trend with red: 1020 nm, green: 1100 nm, blue: 1180 nm. D) average locally corrected emissivity spectrum of each of the subregions with error bars indicating the standard deviation. Purple: Penardum Linea consisting of relatively radar bright plains with ridges and grooves and plains with shields. Blue: Radar bright plains with ridges and grooves. Teal: Molpadia Linea consisting of relatively radar bright, densely lineated plains, plains with shields, and plains with ridges and grooves. Green: Relatively dark plains with wrinkle ridges postdating the Lineae. Yellow: Mylitta Fluctus, postdating plains with wrinkle ridges. Red: Northern part of Kaiwan Fluctus, postdating plains with wrinkle ridges. Geologic interpretation is following [Ivanov and Head \(2001, 2006\)](#). Solid black line and grey area illustrate the reference emissivity $0.8 \pm 1\sigma$ for each band.

is thus not marked by a significant change in spectral shape.

In Lavinia Planitia the locally corrected emissivity maps (Fig. 12) show less significant deviations from the trend, however there are also large scale trends that might be due to gradual changes in the atmosphere or observation parameters. For a better visualization we remove a fitted second order polynomial of latitude and longitude from the data, an approach similarly applied by [Stofan et al. \(2016\)](#) and [Kappel et al. \(2016\)](#). The resulting false color map and spectra of selected region are shown in Fig 14.

There is a marginally significant increase in emissivity at 1020 nm at Molpadia (teal outline) and Penardum Lineae (purple outline), as well as at topographically elevated, radar bright plains at approximately -8°E , -44°S (blue outline). The latter shows inhomogeneous emissivity, but this might be attributed to possible altimetry artifacts appearing as 'pits' at the edge of the elevated terrain (see [Mueller et al., 2008](#),

Fig.14) that are more frequent in the south.

In the false color map the Lineae appear as orange hue that is distinct from the background. The average spectra of these two regions appear similar although they appear at different surface elevations, thus this cannot be simply explained by a residual of the topography correction. [Ivanov and Head \(2001\)](#) map all these as densely lineated plains, shield plains and ridged and grooved plains, all predating the surrounding plains with wrinkle ridges. The spectral shape (false color hue) appears more similar to the Sabin crater ejecta than the more recent volcanic units in Themis Regio. The increase in the 1100 nm band (green channel) that distinguishes the more orange hue from the reddish hue of the volcanic features is less significant than that of the 1020 nm band.

The Linea are locally not the most recently formed units and therefore an interpretation of the increased emissivity as less chemically weathered surfaces of the same primary composition as in Themis Regio ([Smrekar et al., 2010](#)) is not appropriate. An alternative interpretation could be a primary mineral composition that forms less low emissivity secondary minerals. Olivines and pyroxenes with high Mg content are expected to be stable while their higher Fe counterparts are expected to react with CO₂ forming silica and iron oxides ([Fegley et al., 1992](#)), which are proposed to form a low emissivity crust ([Smrekar et al., 2010](#)). Another proposed secondary mineral is anhydrite ([Fegley and Prinn, 1989](#)), which might not form from rocks with comparatively low Ca content.

6. Discussion

Our approach provides a globally consistent inversion of radiance to surface emissivity with results similar to the emissivity retrievals of [Kappel et al. \(2016\)](#) in Themis Regio. As [Kappel et al. \(2016\)](#) we find a systematic increase of emissivity of approximately 0.05 per kilometer of elevation in the 1020 nm window. As discussed and modeled by [Kappel et al. \(2016\)](#), there are a number of factors that can affect such a trend, including unknown phenomena in the lower atmosphere of Venus such as aerosols or deviations of the surface temperature from our assumptions. When that trend is statistically removed the same geologic features show significant anomalies in the 1020 nm band. These anomalies were also present in the purely statistical data reduction presented by [Stofan et al. \(2016\)](#).

Aside of incorrect assumptions in the radiative transfer modeling, it is conceivable that emissivity does change systematically with elevation due to temperature dependent chemical weathering as seen in the radiothermal emissivity ([Klose et al., 1992](#)) and thus that the statistical removal of the trend is unwarranted. However, in our global map there are other regions on the same latitude (e.g. Lavinia Planitia) with a different trend with a significantly different gradient of about 0.03 per km.

There is no indication that the Lavinia Planitia region has an overall different primary composition that could result in a different trend of secondary minerals with elevation. Both the regional plains with

wrinkle ridge in the basin as well as the stratigraphically younger, not tectonically deformed, massive lava flow fields emanating from the extensional belt surrounding the basin show the same, less steep trend. It seems far-fetched to propose that the lava in these two dissimilar settings have some common but unusual composition different from the rest of the hemisphere observed by VIRTIS.

We find qualitatively similar trends with larger amplitude in the other bands at 1100 and 1180 nm, which is different from the retrievals by Kappel et al. (2016). The emissivity trend in the work of Kappel et al. (2016) changes sign in the 1100 nm window and is small in the 1180 nm window. A possible cause for this difference is the treatment of unknown CO₂ continuum opacity. We assume a CIA coefficient that relates to the square of molecular number density and fit a value to the whole dataset assuming an average emissivity value. The fitted CIA values are roughly consistent with the work of Bézard et al. (2009, 2011) and Fedorova et al. (2015), remaining differences can probably be attributed to the fact that these works only fit the gradient of observed radiance with respect to topography, not the absolute values as we do. Our work shows that the gradient of radiance depends on location due to some unknown effect, these works therefore might not have found the correct value for CIA, even though their results are close to room temperature laboratory measurements (Snels et al., 2014b).

The choice of emissivity for our fit of CIA affects the derived emissivity trend, but only unphysical emissivities beyond unity would result in a significant reduction of the trend for the 1020 nm window. The fact that we see different trends in different locations also indicates that a universal factor such as the CO₂ opacity is not solely responsible, i.e. that the trend is not an artifact from the adoption of an incorrect continuum. Incorrect CO₂ opacity can introduce a trend in derived emissivity but not different trends in different locations.

In case of a real deviation from model assumptions on temperature, we would expect to see a similar trend in all bands. Assuming that this is the case we can only speculate why Kappel et al. (2016) see different trends in different bands. (Kappel et al., 2016) use the same temperature profile but fit their data with a larger number of atmospheric parameters to a larger number of bands. Uncertainties in calibration parameters such as detector sensitivity or straylight spectral shape could interfere with the fits in both our and their model. For example an overestimate of the straylight intensity could result in a lower radiance that would be compensated by fitting of a higher continuum coefficient. The first principal component of the straylight used by Kappel et al. (2012, Fig. 9) seems to have a peak near 1100 nm that is absent in our spectral straylight shape (see appendix AppendixA.2).

Kappel et al. (2016) note that their approach to modeling the unknown absorption continuum is not directly comparable to that of other authors (e.g. Bézard et al., 2011; Fedorova et al., 2015; Snels et al., 2014b), but there is a difference in the relative values of the fitted continuum between the windows. The ratio of the fitted continuum coefficients of the 1100 and 1180 nm window relative to that of the 1020 nm window is 5.5 and 4.5, respectively, in our work, and 9.7 and 4.9 in the work of Kappel et al. (2016). A

too high continuum would result in our approach in an underestimate of model radiance at lower elevations, corresponding to a trend of emissivity decreasing with surface elevation, as observed in the 1100 nm emissivities retrieved by (Kappel et al., 2016).

All in all we find that the emissivity trend is most likely caused by deviation of surface temperature from the VIRA temperature model. The VIRTIS data set might be used to develop an improved model of the near surface temperature. This would be impacted by the uncertainty of the continuum opacity, but it should be noted that a globally constant temperature lapse rate likely cannot explain the observations. It would be necessary to fit near surface temperature models regionally. To choose the size of regions well, physical constraints on the possible vertical and lateral temperature variations near the surface are required.

Kappel et al. (2015) note that numerical models of atmospheric dynamics with self-consistent temperatures (Lebonnois et al., 2010) show deviations from the VIRA model. The fact that the trend varies between an isolated highland in Themis Regio and basin surrounded by highlands in Lavinia Planitia suggests that interaction of atmospheric circulation with topography might be responsible. We can exclude cooling over night as a cause for this phenomenon, since the data actually indicate an increase with average local time of observation.

Regardless of the cause of the trend, it is not an unsurmountable obstacle to geologic interpretation of the derived emissivity maps. We can confirm the trend at 1020 nm wavelength is consistent over length scales of 1000 km, with 2σ standard deviations as small as 0.02 relative to a single trend function. This confirms the assumptions about lower atmosphere parameter correlation lengths in the emissivity error calculations of (Kappel et al., 2015). Some of the variation can likely be attributed to variability of instrumental factors such as noise and residual straylight. For geologic interpretation the derived emissivity maps presented here have to be locally corrected for the trend, as was done by Basilevsky et al. (2012), Stofan et al. (2016) and Kappel et al. (2016). We have performed this correction using SAR images and geologic interpretation as guide to select reference regions that provide a well defined trend.

The trend is non-linear, thus a linear correction as in the work of (Kappel et al., 2016) would result in some higher order residuals with respect to topography. Nevertheless, we can essentially reproduce the map at 1020 nm of Themis Regio by (Kappel et al., 2016), and the purely statistical data reduction in (Stofan et al., 2016). The significantly different trend in Lavinia Planitia shows that each region that is to be interpreted in terms of geology has to be corrected individually, but the consistency of the trend over regional scales provides a similar precision as the more detailed calculations of (Kappel et al., 2016).

Assuming that there is no real trend of emissivity with topography, but instead a different temperature profile or unaccounted opacity in the lowest atmosphere has implications for the emissivity of topographic slopes owing to the blurring described in section 4.3.1. Our model overestimates the TOA radiance of lowlands, and therefore the weighted average of radiance (Eq. 2) on slopes is also overestimated. This means that emissivity derived from this model is underestimated at these locations. The regional correction

of emissivity does not include the information about topographic variance within the blurring distance and therefore cannot fully correct for this. It can be corrected by accepting the hypothesis that either the assumed temperature or atmospheric opacity are incorrect, adjusting the model to fit the data and iterating the process. As discussed before, adjusting the model further, e.g. with regionally varying atmospheric temperatures, is beyond the scope of this work.

This inaccuracy is small compared to the overall uncertainty. We have derived emissivity maps using a pre-calculated blurred topography which uses a fit to the data from [Mueller et al. \(2008\)](#) in Eqs. 2 and Eqs. 3 as in the work of [Smrekar et al. \(2010\)](#); [Gilmore et al. \(2015\)](#); [Stofan et al. \(2016\)](#) and [Kappel et al. \(2012, 2016\)](#) and found only small differences to the results presented here.

Our results are consistent with the high emissivity reported by [Smrekar et al. \(2010\)](#); [Stofan et al. \(2016\)](#). In our map of the 1020 nm emissivity, all emissivity features in Themis Regio that [Stofan et al. \(2016\)](#) interpret as plausible sites of recent volcanism show at least an $1\text{-}\sigma$ increase over the reference regions (Table 1). These volcanic features tend to have a wider range of elevations within the blurring radius than typically found in the plains and therefore the true emissivity is likely slightly higher.

As in the work of [Stofan et al. \(2016\)](#) and [Kappel et al. \(2016\)](#), the emissivity of the top of Shiwanokia Corona is lower than the reference region, located on the neighboring corona Shulamite. These coronae are associated with plateaus that are wide compared to the blurring function, and therefore inaccuracies due to blurring cannot be responsible for these emissivity differences.

The high emissivity of Mylitta Fluctus in Lavinia Planitia reported by [Helbert et al. \(2008\)](#) is an artifact of the variation of emissivity trends. The 1100 and 1180 nm bands have large uncertainty as expected based on the work of [Kappel et al. \(2015\)](#), and therefore do not indicate significant variation of the surface spectrum.

Our use of the maximum standard deviation from all topography bins averaging over all reference regions as error estimate very likely strongly underestimates the significance of the anomalies. Instrumental errors are correlated over either one VIRTIS pixel, typically 20 km, in case of detector noise, or one VIRTIS image in case of straylight or wavelength registration errors, which typically covers the surface over several thousand km distance. Atmospheric errors have correlation lengths on the order of 1000 km ([Kappel et al., 2015](#)). We construct the reference emissivity trend from regions spread out over such large distances and therefore the variance is affected by these large scale errors in addition to any instrumental noise. The anomalies that are correlated with geologic features are however typically on the scale of a few hundred km. The only source that can introduce errors correlated on that spatial scale is the topography data, which is indeed problematic in areas with steep slopes due to the low resolution of the Magellan data ([Mueller et al., 2008](#)).

7. Conclusions

Our results demonstrate both the challenges and promise of infrared spectroscopy on Venus. The fact that different regions require different atmospheric corrections show that our model of the lower atmosphere (Seiff et al., 1985) is incomplete, but also that infrared data provide an opportunity to enhance our knowledge in that regard. We show that there are marginally significant emissivity variations that can be plausibly interpreted in terms of surface composition and chemical weathering (Smrekar et al., 2010). In the present analysis we cannot show that there are significant variations of spectral shape. This is because we cannot easily disentangle variance due to large scale errors affecting our uncertainty estimate from actual emissivity anomalies. The choice of large reference regions that result in a large uncertainty estimates is to demonstrate that there are distinct trends in different regions, that are however consistent over thousands of kilometers.

For geologic analysis it would be preferable to select smaller references regions close to the regions of interest, so that large scale errors affect both similarly. Statistical tests such as employed by Gilmore et al. (2015) would then show whether there are significant changes of the emissivity spectrum between the two or more regions. With the present analysis we can show that the top of Shiwanokia Corona, as in previous studies (Stofan et al., 2016; Kappel et al., 2016) has significantly lower emissivity in all three bands when compared to the top of Shulamite Corona, 500 km to the North-East. The trend seems to be consistent over such distances thus this is unlikely to be an effect of varying atmospheric temperature.

In this study we omitted the tessera regions (Hashimoto et al., 2008; Gilmore et al., 2015), because there are strong indications that the radar altimetry of this terrain is unreliable (Mueller et al., 2008). Errors in altimetry would however present as a specific deviation of emissivity in all three bands and we will use this to test the tessera regions for altimetry errors in future.

VIRTIS on Venus Express is the flight spare of a hyperspectral imager for the Rosetta comet orbiter (Coradini et al., 1998) and was not optimized for observations of the nightside of Venus. The Venus Express mission was focused on atmosphere observations (Drossart et al., 2007). An instrument and mission specifically designed for this task could provide much improved instrumental straylight suppression, spectral calibration stability and signal to noise ratio (Helbert et al., 2016), as well as systematically map most of the planet. Maybe more importantly it would be able to observe in the sub-micrometer wavelengths (Baines et al., 2000) where two additional windows with low radiance -but also low atmospheric opacity comparable to the 1020 nm band- would provide much better constraints on surface spectral signatures. Laboratory emissivity spectra acquired at Venus temperatures demonstrate the ability to distinguish major rock types as well as weathering products using the wavelengths that can be observed through the atmosphere of Venus (Helbert et al., 2018; Dyar et al., 2017).

8. Acknowledgments

The Venus Express VIRTIS data are archived at the Planetary Science Archive of the European Space Agency, accessible at <https://archives.esac.esa.int/>. The Magellan data is archived at the NASA PDS at <http://pds-geosciences.wustl.edu/missions/magellan/>. The improved version of the Magellan GTDR prepared by Rappaport et al. (1999) can be found at ftp://voir.mit.edu/pub/mg_3003/. The authors are working with NASA’s Planetary Data System to archive data from this study. We acknowledge the work of the VIRTIS Principal Investigators Pierre Drossart and Giuseppe Piccioni and the financial support for the instrument by CNES and ASI. Parts of this work were carried out at the Jet Propulsion Laboratory, California Institute of Technology, using funds from NASA’s Planetary Mapping and Data Analysis Program.

Appendix A. Processing of VIRTIS calibrated spectra

Appendix A.1. Even odd correction

The even odd effect correction has to be done on raw, uncalibrated data. The calibration is described by Cardesin Moinelo et al. (2010). The main step converts the recorded raw data digital number counts D to the calibrated radiance I_{cal} by

$$I_{\text{cal}} = \frac{D}{S t_{\text{exp}}} \quad (\text{A.1})$$

where D is the raw data count of the detector pixel corrected for dark current count, S is the instrument transfer function (ITF) and t_{exp} is the integration (exposure) time of the readout. The instrument transfer function is represented by an array of values corresponding to the detector pixels, with dimensions $b \times s$.

The dark current correction is performed by taking observations with the instrument cover closed typically once every 21 lines. As described in the Cardesin Moinelo et al. (2010) the dark current is linearly interpolated between the dark lines and subtracted:

$$D = D_{\text{raw}} - D_{\text{dark}} \quad (\text{A.2})$$

The detector read-out electronics behavior is not perfectly linear as assumed by the above equation, resulting in deviations of the calibrated spectra, typically alternating in sign between even and odd bands. This deviation is called the even odd effect (Cardesin Moinelo et al., 2010; Kappel et al., 2012) and is thought to be related to the ‘the nonsymmetrical clock feedthrough of the read-out integrated circuit’ (Cardesin Moinelo et al., 2010).

Kappel et al. (2012) characterize the even odd effect in the form of correction curves as functions of band, sample and raw data count D_{raw} , affecting both science and dark counts. The convolution of spectra with

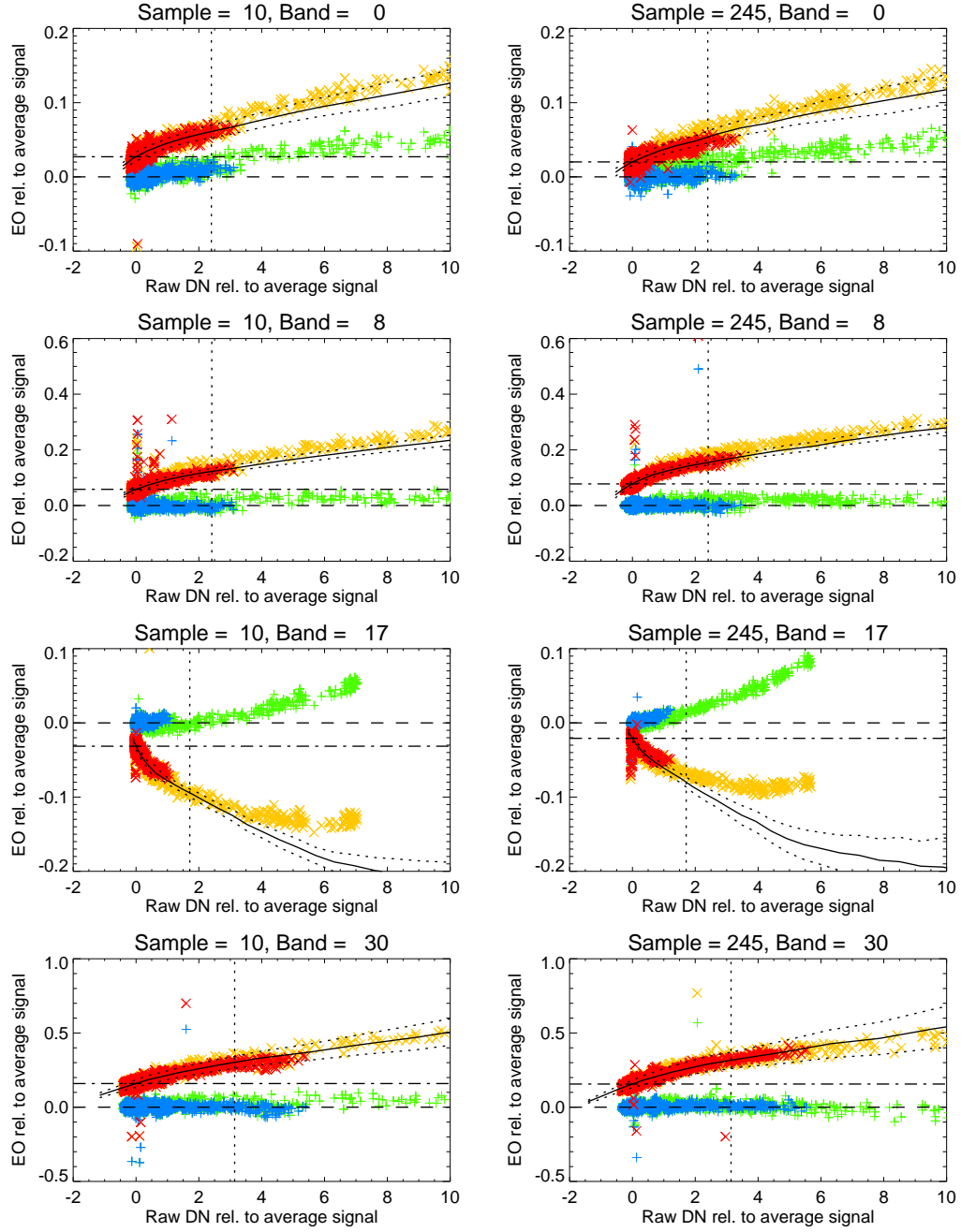


Figure A.15: Validation of the even odd correction exemplified for some bands and samples. The solid curve is the even odd correction curve $EOF(D_{\text{raw}})$ with the dotted curves indicating the EO standard deviation. The dash dotted line is the average $EOF(D_{\text{dark}})$. EO estimates Eq.(A.3) of spectra showing space (offset by their individual $EOF(D_{\text{dark}})$ for clarity) are indicated by \times symbols in red and orange for high and low minimum solar incidence angle, respectively. $+$ symbols show the space spectra after even odd correction, with blue and green colors indicating high and low incidence angle, respectively. All values are offset and scaled as ratio to the signal of nightside spectra as described in the text. Vertical dotted line indicates a value greater than 99% of nightside radiances.

a kernel (ker_5) reduces the even odd effect. The difference to the original spectrum provides an estimate of the amplitude EO effect.

Following the approach of Kappel et al. (2012) we derive corrections for the non-linear behavior of the detector from raw dayside spectra with a shorter exposure duration than the nightside spectra. Dayside spectra have fewer spectral features and using shorter exposure times samples the same range of absolute detector counts as longer exposure nighttime data. The correction curves are based on the difference of the dark corrected raw spectrum to the ker_5 smoothed spectrum:

$$EO = D - D * ker_5 \quad (A.3)$$

We found no better approach than the assumption of Kappel et al. (2012), that EO can be predicted as a function of raw detector count uncorrected for dark current D_{raw} . One alternative is to define the even odd measure based on the uncorrected count (i.e. as $D_{\text{raw}} - D_{\text{raw}} * ker_5$) but this results in a larger scatter of EO . This means that there are unknown factors that offset the amplitude of the even odd effect, but this offset is mostly accounted for by the dark correction. As discussed by Kappel et al. (2012) and based on our own analysis it seems that instrument temperature might have an effect but none of the available instrument housekeeping temperature sensors provides a good predictor.

As in the work of Kappel et al. (2012), the correction curve is derived by determining the average of EO values in regular D_{raw} intervals (bins) using only spectra with a dark raw count D_{dark} within ± 10 DN of the median D_{dark} . All VIRTIS spectra of the planetary disk with a exposure duration $t_{\text{exp}} = 0.36$ s and an solar incidence angle less than 93 deg are used for this statistic. The result is a series of $\langle EO \rangle_i$ and $\langle D_{\text{raw}} \rangle_i$ pairs, where i identifies the D_{raw} bin. The series of these average EO values is different for each detector pixel. The series are used to define the correction functions $EOF(D_{\text{raw}})$ via interpolation.

These series trend towards zero at the median D_{dark} of the $t_{\text{exp}}=0.36$ sec set of dayside spectra because the dark correction eliminates the even odd effect for zero radiance. To use the correction to predict the even odd deviation of nightside spectra requires adjusting for the higher dark count that comes with the longer exposure durations. The even odd corrected detector count DN is therefore

$$D_{EO} = D - [EOF(D_{\text{raw}}) - EOF(D_{\text{dark}})] \quad (A.4)$$

We use 3.3 sec space spectra with some non in-field straylight to validate and illustrate this procedure in Fig. A.15. The even odd effect can be well measured with these spectra and if their EO is offset by the value $EOF(D_{\text{dark}})$ that has already been corrected for by the dark subtraction it lines up with the EOF curves. Accordingly, the even odd corrected data show deviations from zero, mostly in bands 0 and 17. Possibly this is due to edge effects in band 0 and the adjacent absorption feature longwards of band 17. These deviations are small compared to the expected signal.

To illustrate the relative deviations we scale the *EO* data in Fig. A.15 to the average signal expected for nightside observations including instrumental straylight. Based on averages of the VIRTIS data set that is I_{cal} of 58, 45, 92 and 14 $\text{mW}\mu\text{m}^{-1}\text{m}^{-2}\text{sr}^{-1}$ for band 0, 8, 17 and 30, respectively. Similarly, the D_{raw} of the x-axis are offset and scaled to the values corresponding to these radiances at average dark counts. That means a value of 0 corresponds to zero radiance and one corresponds to average radiance.

Fig. A.15 shows that the EO effect can be corrected for, but this has to be done on a per detector pixel basis. Deviations from zero of the corrected (blue and green) data are small to the left of the vertical line indicating the 99th percentile of data, indicating that the residual EO effect is a small fraction of the signal. Within the range 99th percentile of the nightside radiances, indicated by a vertical line in Fig. A.15, the residual *EO* of corrected data (+ symbols) the error is typically $<5\%$ of expected average radiances. Larger deviations occur outside of the range of radiances useful for nightside observations.

The data indicate that viewing geometry has an impact. The colors in Fig. A.15 represent different selections of the data, with blue and red indicating spectra with a high minimum solar incidence angle on the same line, i.e. an instantaneous FOV far from the terminator, and the green and orange indicating spectra closer to the terminator.

Appendix A.2. Straylight correction

Most VIRTIS spectra show some straylight in addition to the thermal emission of Venus. As discussed by Kappel et al. (2012) there are several possible sources. One source is Venus twilight that is detectable up to a solar incidence angle of at least 95° . We exclude data with solar incidence angles $< 98^\circ$.

The most important for these southern hemisphere observations is reflected light from the dayside of Venus that is scattered off the designed optical path within the instrument. There are spectral regions where Venus emission is negligible and all the observed light can be attributed to straylight. If the spectral shape of straylight is known, it can be scaled to match observations at these emission free wavelengths and then subtracted from the whole spectrum. Mueller et al. (2008) derive the spectral shape by fitting a linear relation of emission window radiance to radiance at an emission free region between 1.36 and 1.39 μm . This has the disadvantage that any coincidental correlation of straylight and emission radiance impacts the estimate of the spectral shape of straylight (Fig. A.16 red dotted graph).

Kappel et al. (2012) use spectra showing space next to the planet (spectrum c in Fig. 2) to investigate the spectral shape using the method of principal component analysis (PCA). Following this approach we select a set of spectra showing space and perform a PCA.

The restrictions for the spectra in the data set are a line of sight with a closest distance of 200 km to the planet's surface to exclude the possibility of light scattered within the upper atmosphere, and that the minimum solar incidence angle of any pixel observing Venus in the same line is greater than 100° in order to preclude dayside or twilight spectra in the same instantaneous field of view.

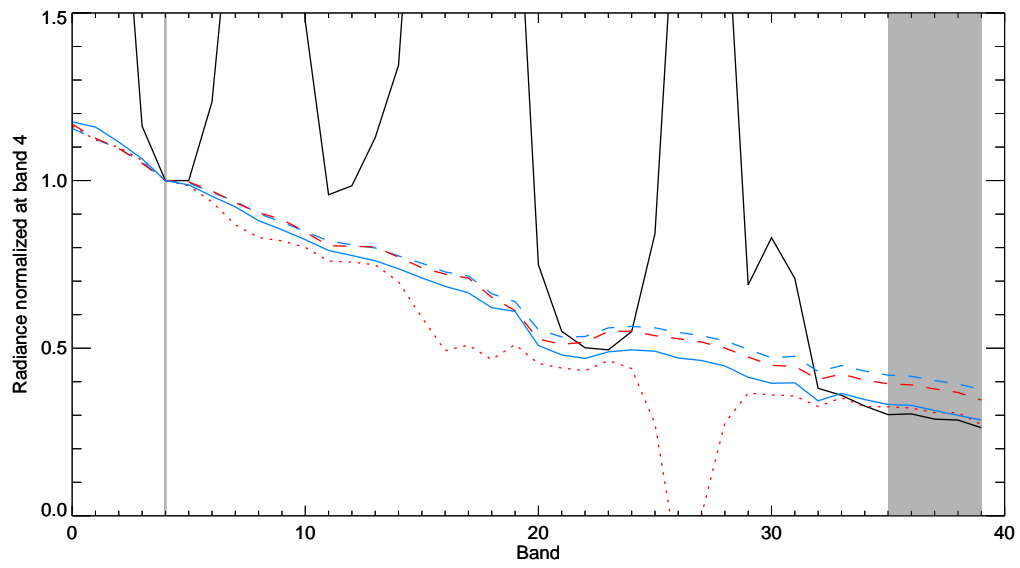


Figure A.16: VIRTIS calibrated data (solid black) include a varying instrumental straylight contribution. Grey vertical bars indicate non-emitting bands used as measure for instrumental straylight, in the following called dark bands. [Mueller et al. \(2008\)](#) made an estimate of straylight by linear regression of nightside radiances versus dark bands (dotted red) but this is affected by coincidental correlation of emission radiance and straylight. The average spectrum of space is pure straylight (dashed red) and shows a different spectral slope. The first component of a PCA of space spectra (dashed blue) is similar to the average of space but in linear combination with the second component fits the nightside well at both dark bands.

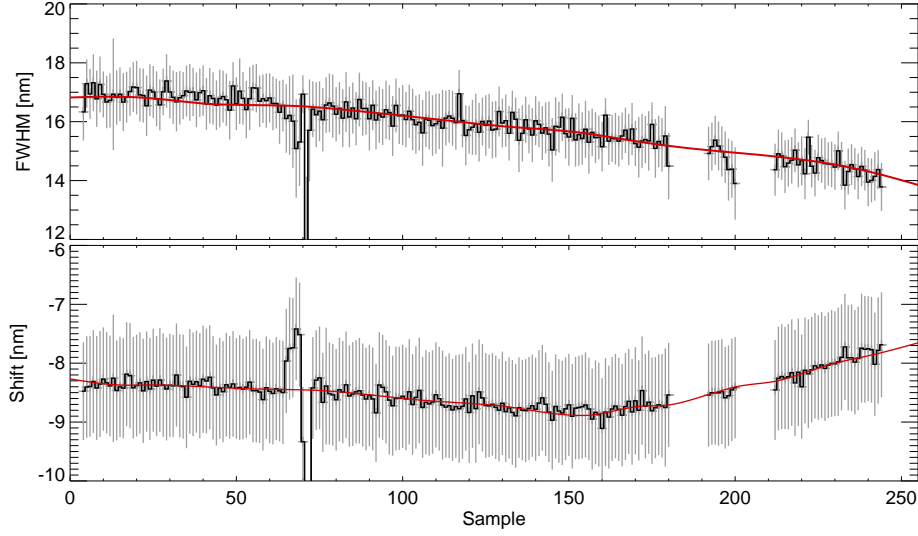


Figure A.17: The black line shows the average bandwidth FWHM and band shifts derived of all VIRTIS spectra fitted with synthetic spectra individually. The error bars correspond to the standard deviation over all fitted data. A steady variation of these curves is expected for this kind of instrument (Cardesin Moineau et al., 2010) but these averages show outlying samples which are probably due to calibration artifacts, e.g. pixels with reduced sensitivity. The red line indicates the smoothed and interpolated series that we force the spectral registration to follow as described in the text.

The result of the PCA, the principal components, are an orthogonal base of spectra that are ordered by their contribution to total variance of space radiance. The first component is a spectrum similar to a dayside spectrum, i.e. increasing with decreasing wavelength and a few absorption features. The second component corresponds in general to a change in spectral slope as its sign changes in the middle of the spectral region. Further components have a comparatively small contribution to the variance of space radiance (as indicated by the corresponding eigenvalue of the covariance matrix).

To apply these spectral shapes derived from the straylight of space observations to the nightside data, we fit a linear combination of the first and second component in the least squares to two radiances of relatively emission free wavelength regions, and subtract the fit. The dark bands are band 4 and the spectral median of bands 35 to 39. An example illustrating this straylight correction is shown in Fig. 3.

Appendix A.3. Spectral calibration update

The spectral calibration of VIRTIS in Venus orbit showed some changes relative to the on ground calibration. The spectral width of the bands is wider than the nominal 10 nm (FWHM) and the band centers were shifted by approximately -6.5 nm (Cardesin Moineau et al., 2010). The spectral calibration included with the VIRTIS archive does not include variation with respect to sample.

A solution is to use the deviation from ground calibration in band centers and widths as free parameters in a fit of synthetic spectra to the individual data spectra (e.g. Bézard et al., 2009; Kappel et al., 2016). We create a preliminary lookup table of synthetic spectra for various surface elevations. The other input variables for the radiative transfer model are for this task fixed at an emissivity of 0.8, a cloud particle mode 2' and 3 density factor of 1.75 and a coefficient for collision induced continuum opacity of $0.26 \times 10^{-9} \text{cm}^{-1} \text{amagat}^{-2}$ for the $1.02 \mu\text{m}$ window, $1.5 \times 10^{-9} \text{cm}^{-1} \text{amagat}^{-2}$ for the $1.10 \mu\text{m}$ window, $1.35 \times 10^{-9} \text{cm}^{-1} \text{amagat}^{-2}$ for the $1.10 \mu\text{m}$ window, and $1.5 \times 10^{-9} \text{cm}^{-1} \text{amagat}^{-2}$ for the $1.31 \mu\text{m}$ window. We choose these values to approximately reproduce the relative intensity of the different window peaks and are different from the final values used for emissivity inversion.

The synthetic spectra are fitted to the observed spectra at bands 4 to 19. This restriction is to avoid the one sided flank of the $1.02 \mu\text{m}$ window and the non-thermal emission at $1.27 \mu\text{m}$ (Crisp et al., 1996; Piccioni et al., 2009). To fit the data, the synthetic spectra with spectral resolution and sampling of 1 nm are convolved with a Gaussian instrumental function with FWHM as parameter Cardesin Moineau et al. (2010), multiplied with a scale factor to allow for cloud opacity (Bézard et al., 2011) and interpolated to the band center wavelengths of VIRTIS offset by the shift parameter. An example of a data and fitted spectrum are shown in Fig. The set of best fitting parameters (bandwidth, scale factor and wavelength shift) are recorded for all spectra.

The parameters of interest are bandwidth and wavelength shift. Almost all of the fitted bandwidths are in the interval of 12 to 20 nm FWHM, with a standard deviation over the whole data set of 1.3 nm, disregarding outliers. Similarly the fitted wavelength shift relative to the original calibration falls mostly in the range -15 to -5 nm, with a standard deviation of 0.9 nm. Approximately 10 % of the data are outliers or could not be fitted.

As expected (Cardesin Moineau et al., 2010) the fitted spectral parameters show a correlation with instrument temperature data and detector *sample*. In an attempt to capture this instrumental behavior and not the noise caused by radiance noise, bad pixel and EO residuals, we do not use the bandwidths and shifts individually fitted to each spectrum but create a more continuous model of the spectral characteristics, which minimizes the deviation between fitted and model values. We calculate the average bandwidth and shift of each *sample* and smooth the data to get more continuous series of the averages, shown in Fig. A.17.

Among the housekeeping (HK) temperature data provided with the VIRTIS raw data, the spectrometer grating temperature, the HK channel 'M_GRATING_TEMP', predicts the bandwidth best. The shift cannot be predicted well with any HK temperature channel, the correlation to the detector temperature (HK channel 'M_IR_TEMP') is the largest but still small.

Based on these observations we consider it possible that bandwidth and shift are affected by thermal stresses in instrument and spacecraft that are not well described by the HK data. Instead we assume that the thermal state varies sufficiently slowly to be near to linear over the duration of one observation. For each

VIRTIS observation we use the band center shifts and bandwidth FWHM values derived from comparison with synthetic spectra to fit a model wavelength registration. The model consists of the sum of the average per sample over all observations (red lines in Fig. A.17) a linear trend with each VIRTIS cube line including a constant offset. The resulting root mean square deviation of fitted shifts and bandwidths and their models are 0.25 nm and 0.5 nm, respectively, about half of the per sample standard deviation (see Fig. A.17).

References

- Arnold, G., Haus, R., Kappel, D., Drossart, P., Piccioni, G., Oct. 2008. Venus surface data extraction from VIRTIS/Venus Express measurements: Estimation of a quantitative approach. *Journal of Geophysical Research (Planets)* 113, E00B10.
- Baer, G., Schubert, G., Bindschadler, D. L., Stofan, E. R., Apr. 1994. Spatial and temporal relations between coronae and extensional belts, northern Lada Terra, Venus. *Journal of Geophysical Research* 99, 8355–8369.
- Baines, K. H., Bellucci, G., Bibring, J.-P., Brown, R. H., Buratti, B. J., Bussolletti, E., Capaccioni, F., Cerroni, P., Clark, R. N., Coradini, A., Cruikshank, D. P., Drossart, P., Formisano, V., Jaumann, R., Langevin, Y., Matson, D. L., McCord, T. B., Mennella, V., Nelson, R. M., Nicholson, P. D., Sicardy, B., Sotin, C., Hansen, G. B., Aiello, J. J., Amici, S., Nov. 2000. Detection of Sub-Micron Radiation from the Surface of Venus by Cassini/VIMS. *Icarus* 148, 307–311.
- Barstow, J., Tsang, C., Wilson, C., Irwin, P., Taylor, F., McGouldrick, K., Drossart, P., Piccioni, G., Tellmann, S., 2012. Models of the global cloud structure on venus derived from venus express observations. *Icarus* 217 (2), 542 – 560.
- Basilevsky, A., Shalygin, E., Titov, D., Markiewicz, W., Scholten, F., Roatsch, T., Kreslavsky, M., Moroz, L., Ignatiev, N., Fiethe, B., Osterloh, B., Michalik, H., 2012. Geologic interpretation of the near-infrared images of the surface taken by the venus monitoring camera, venus express. *Icarus* 217 (2), 434 – 450.
- Bézard, B., de Bergh, C., Crisp, D., Maillard, J.-P., Jun. 1990. The deep atmosphere of Venus revealed by high-resolution nightside spectra. *Nature* 345, 508–511.
- Bézard, B., Fedorova, A., Bertaux, J.-L., Rodin, A., Korabev, O., Nov. 2011. The 1.10- and 1.18- μm nightside windows of Venus observed by SPICAV-IR aboard Venus Express. *Icarus* 216, 173–183.
- Bézard, B., Tsang, C. C. C., Carlson, R. W., Piccioni, G., Marcq, E., Drossart, P., May 2009. Water vapor abundance near the surface of Venus from Venus Express/VIRTIS observations. *Journal of Geophysical Research (Planets)* 114, E00B39.
- Bridges, N. T., McGill, G. E., 2002. Geologic Map of the Kaiwan Fluctus Quadrangle (V-44), Venus. U.S. Geological Survey, Geologic Investigation Series I-2747.
- Campbell, D. B., Stacy, N. J. S., Newman, W. I., Arvidson, R. E., Jones, E. M., Musser, G. S., Roper, A. Y., Schaller, C., Oct. 1992. Magellan observations of extended impact crater related features on the surface of Venus. *Journal of Geophysical Research* 97, 16249.
- Cardesin Moinelo, A., Piccioni, G., Ammannito, E., Filacchione, G., Drossart, P., Sep. 2010. Calibration of Hyperspectral Imaging Data: VIRTIS-M Onboard Venus Express. *IEEE Transactions on Geoscience and Remote Sensing* 48, 3941–3950.
- Carlson, R. W., Baines, K. H., Kamp, L. W., Weissman, P. R., Smythe, W. D., Ocampo, A. C., Johnson, T. V., Matson, D. L., Pollack, J. B., Grinspoon, D., Sep. 1991. Galileo infrared imaging spectroscopy measurements at Venus. *Science* 253, 1541–1548.
- Colin, L., 1983. Venus. University of Arizona Press, Tucson, Arizona , Ch. Basic facts about Venus, pp. 10–26.
- Coradini, A., Capaccioni, F., Drossart, P., Semery, A., Arnold, G., Schade, U., Angrilli, F., Barucci, M. A., Bellucci, G., Bianchini, G., Bibring, J. P., Blanco, A., Blecka, M., Bockelee-Morvan, D., Bonsignori, R., Bouye, M., Bussolletti, E., Capria, M. T., Carlson, R., Carsenty, U., Cerroni, P., Colangeli, L., Combes, M., Combi, M., Crovisier, J., Dami, M., DeSanctis, M. C., DiLellis, A. M., Dotto, E., Encrenaz, T., Epifani, E., Erard, S., Espinasse, S., Fave, A., Federico, C., Fink, U., Fonti, S., Formisano, V., Hello, Y., Hirsch, H., Huntzinger, G., Knoll, R., Kouach, D., Ip, W. H., Irwin, P., Kachlicki,

J., Langevin, Y., Magni, G., McCord, T., Mennella, V., Michaelis, H., Mondello, G., Mottola, S., Neukum, G., Orofino, V., Orosei, R., Palumbo, P., Peter, G., Pforte, B., Piccioni, G., Reess, J. M., Ress, E., Saggin, B., Schmitt, B., Stefanovitch, Stern, A., Taylor, F., Tiphene, D., Tozzi, G., Oct. 1998. Virtis : an imaging spectrometer for the rosetta mission. *Planetary and Space Science* 46, 1291–1304.

Crisp, D., Sep. 1986. Radiative forcing of the Venus mesosphere. I - Solar fluxes and heating rates. *Icarus* 67, 484–514.

Crisp, D., Meadows, V. S., Bézard, B., de Bergh, C., Maillard, J.-P., Mills, F. P., 1996. Ground-based near-infrared observations of the Venus nightside: 1.27- μm $\text{O}_2(\text{a}\Delta_g)$ airglow from the upper atmosphere. *Journal of Geophysical Research* 101, 4577–4594.

D’Incecco, P., Müller, N., Helbert, J., D’Amore, M., Feb. 2017. Idunn Mons on Venus: Location and extent of recently active lava flows. *Planetary and Space Science* 136, 25–33.

Drossart, P., Piccioni, G., Adriani, A., Angrilli, F., Arnold, G., Baines, K. H., Bellucci, G., Benkhoff, J., Bézard, B., Bibring, J.-P., Blanco, A., Blecka, M. I., Carlson, R. W., Coradini, A., di Lellis, A., Encrenaz, T., Erard, S., Fonti, S., Formisano, V., Fouchet, T., Garcia, R., Haus, R., Helbert, J., Ignatiev, N. I., Irwin, P. G. J., Langevin, Y., Lebonnois, S., Lopez-Valverde, M. A., Luz, D., Marinangeli, L., Orofino, V., Rodin, A. V., Roos-Serote, M. C., Saggin, B., Sanchez-Lavega, A., Stam, D. M., Taylor, F. W., Titov, D., Visconti, G., Zambelli, M., Hueso, R., Tsang, C. C. C., Wilson, C. F., Afanasenko, T. Z., Oct. 2007. Scientific goals for the observation of Venus by VIRTIS on ESA/Venus express mission. *Planetary and Space Science* 55, 1653–1672.

Dyar, M. D., Helbert, J., Boucher, T., Wendler, D., Walter, I., Widemann, T., Marcq, E., Maturilli, A., Ferrari, S., D’Amore, M., Müller, N., Smrekar, S., Nov. 2017. Mapping Venus Mineralogy and Chemistry In Situ from Orbit with Six-Window VNIR Spectroscopy. *LPI Contributions* 2061, 8004.

Ekonomov, A. P., Golovin, Y. M., Moshkin, B. E., Jan. 1980. Visible radiation observed near the surface of Venus - Results and their interpretation. *Icarus* 41, 65–75.

Erard, S., Drossart, P., Piccioni, G., Jan. 2009. Multivariate analysis of Visible and Infrared Thermal Imaging Spectrometer (VIRTIS) Venus Express nightside and limb observations. *Journal of Geophysical Research (Planets)* 114, E00B27.

Fedorova, A., Bézard, B., Bertaux, J.-L., Korablev, O., Wilson, C., Aug. 2015. The CO_2 continuum absorption in the 1.10- and 1.18- μm windows on Venus from Maxwell Montes transits by SPICAV IR onboard Venus express. *Planetary and Space Science* 113, 66–77.

Fegley, B., Prinn, R. G., Jan. 1989. Estimation of the rate of volcanism on Venus from reaction rate measurements. *Nature* 337, 55–58.

Fegley, B., Treiman, A. H., Sharpton, V. L., 1992. Venus surface mineralogy - Observational and theoretical constraints. In: G. Ryder & V. L. Sharpton (Ed.), *Lunar and Planetary Science Conference Proceedings*. Vol. 22. pp. 3–20.

Ford, P. G., Pettengill, G. H., Aug. 1992. Venus topography and kilometer-scale slopes. *Journal of Geophysical Research* 97, 13103.

Fukuhara, T., Futaguchi, M., Hashimoto, G. L., Horinouchi, T., Imamura, T., Iwagaimi, N., Kouyama, T., Murakami, S.-Y., Nakamura, M., Ogohara, K., Sato, M., Sato, T. M., Suzuki, M., Taguchi, M., Takagi, S., Ueno, M., Watanabe, S., Yamada, M., Yamazaki, A., Jan. 2017. Large stationary gravity wave in the atmosphere of Venus. *Nature Geoscience* 10, 85–88.

Gilmore, M. S., Mueller, N., Helbert, J., Jul. 2015. VIRTIS emissivity of Alpha Regio, Venus, with implications for tessera composition. *Icarus* 254, 350–361.

Grinspoon, D. H., Pollack, J. B., Sittton, B. R., Carlson, R. W., Kamp, L. W., Baines, K. H., Encrenaz, T., Taylor, F. W., Jul. 1993. Probing Venus’s cloud structure with Galileo NIMS. *Planetary and Space Science* 41, 515–542.

Hashimoto, G. L., Imamura, T., Dec. 2001. Elucidating the Rate of Volcanism on Venus: Detection of Lava Eruptions Using Near-Infrared Observations. *Icarus* 154, 239–243.

Hashimoto, G. L., Roos-Serote, M., Sugita, S., Gilmore, M. S., Kamp, L. W., Carlson, R. W., Baines, K. H., Dec. 2008. Felsic

highland crust on Venus suggested by Galileo Near-Infrared Mapping Spectrometer data. *Journal of Geophysical Research (Planets)* 113, E00B24.

Hashimoto, G. L., Sugita, S., Sep. 2003. On observing the compositional variability of the surface of Venus using nightside near-infrared thermal radiation. *Journal of Geophysical Research (Planets)* 108, 13–18.

Haus, R., Arnold, G., Oct. 2010. Radiative transfer in the atmosphere of Venus and application to surface emissivity retrieval from VIRTIS/VEX measurements. *Planetary and Space Science* 58, 1578–1598.

Haus, R., Kappel, D., Arnold, G., Apr. 2014. Atmospheric thermal structure and cloud features in the southern hemisphere of Venus as retrieved from VIRTIS/VEX radiation measurements. *Icarus* 232, 232–248.

Helbert, J., Maturilli, A., Dyar, M. D., Ferrari, S., Mueller, N., Smrekar, S., Mar. 2017. First Set of Laboratory Venus Analog Spectra for All Atmospheric Windows. In: *Lunar and Planetary Science Conference*. Vol. 48. p. 1512.

Helbert, J., Maturilli, A., Dyar, M. D., Ferrari, S., Mueller, N., Smrekar, S., Mar. 2018. Orbital Spectroscopy of the Surface of Venus. In: *Lunar and Planetary Science Conference*. Vol. 49 of *Lunar and Planetary Inst. Technical Report*. p. 1219.

Helbert, J., Müller, N., Kostama, P., Marinangeli, L., Piccioni, G., Drossart, P., Jun. 2008. Surface brightness variations seen by VIRTIS on Venus Express and implications for the evolution of the Lada Terra region, Venus. *Geoph. Res. Lett.* 35, 11201.

Helbert, J., Wendler, D., Walter, I., Widemann, T., Marcq, E., Guignan, G., Ferrari, S., Maturilli, A., Mueller, N., Kappel, D., Jaenchen, J., D’Amore, M., Boerner, A., Dyar, D., Arnold, G., Smrekar, S., 2016. The Venus Emissivity Mapper (VEM) concept. *SPIE Proceedings* 9973, *Infrared Remote Sensing and Instrumentation XXIV*, 99730R.

Irwin, P. G. J., May 1997. Temporal and spatial variations in the Venus mesosphere retrieved from pioneer Venus OIR. *Advances in Space Research* 19, 1169–1179.

Ivanov, M. A., Head, J. W., I., 2001. Geologic Map of the Lavinia Planitia Quadrangle(V55), Venus. U.S. Geological Survey, Geologic Investigation Series I-2684.

Ivanov, M. A., Head, J. W., I., 2006. Geologic Map of the Mylitta Fluctus Quadrangle (V-61), Venus. USGS Scientific Investigations Map 2920.

Kamp, L. W., Taylor, F. W., Calcutt, S. B., Nov. 1988. Structure of Venus’s atmosphere from modelling of night-side infrared spectra. *Nature* 336, 360–362.

Kappel, D., Jan. 2014. MSR, a multi-spectrum retrieval technique for spatially-temporally correlated or common Venus surface and atmosphere parameters. *Journal of Quantitative Spectroscopy & Radiative Transfer* 133, 153–176.

Kappel, D., Arnold, G., Haus, R., Feb. 2016. Multi-spectrum retrieval of Venus IR surface emissivity maps from VIRTIS/VEX nightside measurements at Themis Regio. *Icarus* 265, 42–62.

Kappel, D., Arnold, G., Haus, R., Piccioni, G., Drossart, P., Jul. 2012. Refinements in the data analysis of VIRTIS-M-IR Venus nightside spectra. *Advances in Space Research* 50, 228–255.

Kappel, D., Haus, R., Arnold, G., Aug. 2015. Error analysis for retrieval of Venus’ IR surface emissivity from VIRTIS/VEX measurements. *Planetary and Space Science* 113, 49–65.

Klose, K. B., Wood, J. A., Hashimoto, A., Oct. 1992. Mineral equilibria and the high radar reflectivity of Venus mountaintops. *Journal of Geophysical Research* 97, 16.

Korablev, O., Fedorova, A., Bertaux, J.-L., Stepanov, A. V., Kiselev, A., Kalinnikov, Y. K., Titov, A. Y., Montmessin, F., Dubois, J. P., Villard, E., Sarago, V., Belyaev, D., Reberac, A., Neefs, E., May 2012. SPICAV IR acousto-optic spectrometer experiment on Venus Express. *Planetary and Space Science* 65, 38–57.

Kouyama, T., Imamura, T., Taguchi, M., Fukuhara, T., Sato, T. M., Yamazaki, A., Futaguchi, M., Murakami, S., Hashimoto, G. L., Ueno, M., Iwagami, N., Takagi, S., Takagi, M., Ogohara, K., Kashimura, H., Horinouchi, T., Sato, N., Yamada, M., Yamamoto, Y., Ohtsuki, S., Sugiyama, K., Ando, H., Takamura, M., Yamada, T., Satoh, T., Nakamura, M., Dec. 2017. Topographical and Local Time Dependence of Large Stationary Gravity Waves Observed at the Cloud Top of Venus. *Geophysical Research Letters* 44, 12.

- 1057 Lebonnois, S., Hourdin, F., Eymet, V., Crespin, A., Fournier, R., Forget, F., Jun. 2010. Superrotation of Venus' atmosphere
1058 analyzed with a full general circulation model. *Journal of Geophysical Research (Planets)* 115, E06006.
- 1059 Lebonnois, S., Schubert, G., Jul. 2017. The deep atmosphere of Venus and the possible role of density-driven separation of CO₂
1060 and N₂. *Nature Geoscience* 10, 473–477.
- 1061 Lecacheux, J., Drossart, P., Laques, P., Deladerriere, F., Colas, F., Jul. 1993. Detection of the surface of Venus at 1.0 micrometer
1062 from ground-based observations. *Planetary and Space Science* 41, 543–549.
- 1063 Magee, K. P., Head, J. W., Jan. 1995. The role of rifting in the generation of melt: Implications for the origin and evolution
1064 of the Lada Terra-Lavinia Planitia region of Venus. *Journal of Geophysical Research* 100, 1527–1552.
- 1065 Magee Roberts, K., Guest, J. E., Head, J. W., Lancaster, M. G., Oct. 1992. Mylitta Fluctus, Venus: Rift-Related, Centralized
1066 Volcanism and the Emplacement of Large-Volume Flow Units. *Journal of Geophysical Research* 97, 15991–16015.
- 1067 Meadows, V. S., Crisp, D., 1996. Ground-based near-infrared observations of the Venus nightside: The thermal structure and
1068 water abundance near the surface. *Journal of Geophysical Research* 101, 4595–4622.
- 1069 Moroz, V. I., Mar. 2002. Estimates of visibility of the surface of Venus from descent probes and balloons. *Planetary and Space*
1070 *Science* 50, 287–297.
- 1071 Mueller, N., Helbert, J., Erard, S., Piccioni, G., Drossart, P., 2012. Rotation period of Venus estimated from Venus Express
1072 VIRTIS images and Magellan altimetry. *Icarus* 217 (2), 474 – 483.
- 1073 Mueller, N., Helbert, J., Hashimoto, G. L., Tsang, C. C. C., Erard, S., Piccioni, G., Drossart, P., Dec. 2008. Venus surface
1074 thermal emission at 1 μm in VIRTIS imaging observations: Evidence for variation of crust and mantle differentiation
1075 conditions. *Journal of Geophysical Research (Planets)* 113, E00B17.
- 1076 Mueller, N. T., Smrekar, S., Helbert, J., Stofan, E., Piccioni, G., Drossart, P., May 2017. Search for active lava flows with
1077 VIRTIS on Venus Express. *Journal of Geophysical Research (Planets)* 122, 1021–1045.
- 1078 Pettengill, G. H., Ford, P. G., Johnson, W. T. K., Raney, R. K., Soderblom, L. A., Apr. 1991. Magellan - Radar performance
1079 and data products. *Science* 252, 260–265.
- 1080 Piccioni, G., Drossart, P., Suetta, E., Cosi, M., Ammannito, E., Barbis, A., Berlin, R., Boccaccini, A., Bonello, G., Bouy, M.,
1081 Capaccioni, F., Cherubini, G., Dami, M., Dupuis, O., Fave, A., Filacchione, G., Hello, Y., Henry, F., Hofer, S., Huntzinger,
1082 G., Melchiorri, R., Parisot, J., Pasqui, C., Peter, G., Pompei, C., Ress, J. M., Semery, A., Soufflot, A., Adriani, A., Angrilli,
1083 F., Arnold, G., Baines, K., Bellucci, G., Benkhoff, J., Bézard, B., Bibring, J.-P., Blanco, A., Blecka, M. I., Carlson, R.,
1084 Coradini, A., Di Lellis, A., Encrenaz, T., Erard, S., Fonti, S., Formisano, V. T., Fouchet, V., Garcia, R., Haus, R., Helbert,
1085 J., Ignatiev, N. I., Irwin, P., Langevin, Y., Lebonnois, S., Lopez Valverde, M. A., Luz, D., Marinangeli, L., Orofino, V.,
1086 Rodin, A. V., Roos-Serote, M. C., Saggini, B., Sanchez-Lavega, A., Stam, D. M., Taylor, F., Titov, D., G., V., Zambelli, M.,
1087 2007. VIRTIS (Visible and Infrared Imaging Spectrometer) for Venus Express. ESA, special publication 1295 Edition.
- 1088 Piccioni, G., Zasova, L., Migliorini, A., Drossart, P., Shakun, A., Garcia Munoz, A., Mills, F. P., Cardesin-Moinelo, A., 2009.
1089 Near-ir oxygen nightglow observed by virtis in the venus upper atmosphere. *Journal of Geophysical Research: Planets*
1090 114 (E5), e00B38.
- 1091 Pieters, C. M., Head, J. W., Patterson, W., Pratt, S., Garvin, J., Dec. 1986. The color of the surface of Venus. *Science* 234,
1092 1379–1383.
- 1093 Pollack, J. B., Dalton, J. B., Grinspoon, D., Wattson, R. B., Freedman, R., Crisp, D., Allen, D. A., Bézard, B., Debergh, C.,
1094 Giver, L. P., Ma, Q., Tipping, R., May 1993. Near-infrared light from Venus' nightside - A spectroscopic analysis. *Icarus*
1095 103, 1–42.
- 1096 Ragent, B., Esposito, L. W., Tomasko, M. G., Marov, M. I., Shari, V. P., 1985. Particulate matter in the Venus atmosphere.
1097 *Advances in Space Research* 5, 85–115.
- 1098 Rappaport, N. J., Konopliv, A. S., Kucinkas, A. B., Ford, P. G., May 1999. An Improved 360 Degree and Order Model of
1099 Venus Topography. *Icarus* 139, 19–31.

1100 Rothman, L., Barbe, A., Benner, D. C., Brown, L., Camy-Peyret, C., Carleer, M., Chance, K., Clerbaux, C., Dana, V., Devi,
1101 V., Fayt, A., Flaud, J.-M., Gamache, R., Goldman, A., Jacquemart, D., Jucks, K., Lafferty, W., Mandin, J.-Y., Massie,
1102 S., Nemtchinov, V., Newnham, D., Perrin, A., Rinsland, C., Schroeder, J., Smith, K., Smith, M., Tang, K., Toth, R.,
1103 Auwera, J. V., Varanasi, P., Yoshino, K., 2003. The hitran molecular spectroscopic database: edition of 2000 including
1104 updates through 2001. *Journal of Quantitative Spectroscopy and Radiative Transfer* 82 (1), 5 – 44, the HITRAN Molecular
1105 Spectroscopic Database: Edition of 2000 Including Updates of 2001.

1106 Rothman, L., Gordon, I., Barber, R., Dothe, H., Gamache, R., Goldman, A., Perevalov, V., Tashkun, S., Tennyson, J.,
1107 2010. Hitemp, the high-temperature molecular spectroscopic database. *Journal of Quantitative Spectroscopy and Radiative*
1108 *Transfer* 111 (15), 2139 – 2150, xVIth Symposium on High Resolution Molecular Spectroscopy (HighRus-2009).

1109 Sagan, C., Jun. 1975. Windblown dust on Venus. *Journal of Atmospheric Sciences* 32, 1079–1083.

1110 Satoh, T., Imamura, T., Hashimoto, G. L., Iwagami, N., Mitsuyama, K., Sorahana, S., Drossart, P., Piccioni, G., Apr. 2009.
1111 Cloud structure in Venus middle-to-lower atmosphere as inferred from VEX/VIRTIS 1.74 μm data. *Journal of Geophysical*
1112 *Research (Planets)* 114, E00B37.

1113 Seidelmann, P. K., Archinal, B. A., A’Hearn, M. F., Cruikshank, D. P., Hilton, J. L., Keller, H. U., Oberst, J., Simon, J. L.,
1114 Stooke, P., Tholen, D. J., Thomas, P. C., Mar. 2005. Report of the IAU/IAG Working Group on Cartographic Coordinates
1115 and Rotational Elements: 2003. *Celestial Mechanics and Dynamical Astronomy* 91, 203–215.

1116 Seiff, A., 1987. Further information on structure of the atmosphere of Venus derived from the VEGA Venus balloon and lander
1117 mission. *Advances in Space Research* 7, 323–328.

1118 Seiff, A., Schofield, J. T., Kliore, A. J., Taylor, F. W., Limaye, S. S., 1985. Models of the structure of the atmosphere of Venus
1119 from the surface to 100 kilometers altitude. *Advances in Space Research* 5, 3–58.

1120 Smrekar, S. E., Stofan, E. R., Mueller, N., Treiman, A., Elkins-Tanton, L., Helbert, J., Piccioni, G., Drossart, P., Apr. 2010.
1121 Recent Hotspot Volcanism on Venus from VIRTIS Emissivity Data. *Science* 328, 605–608.

1122 Snels, M., Stefani, S., Grassi, D., Piccioni, G., Adriani, A., Nov. 2014a. Carbon dioxide opacity of the Venus’ atmosphere.
1123 *Planetary and Space Science* 103, 347–354.

1124 Snels, M., Stefani, S., Piccioni, G., Bézard, B., Jan. 2014b. Carbon dioxide absorption at high densities in the 1.18 μm nightside
1125 transparency window of Venus. *Journal of Quantitative Spectroscopy & Radiative Transfer* 133, 464–471.

1126 Stefani, S., Piccioni, G., Snels, M., Grassi, D., Adriani, A., Mar. 2013. Experimental CO₂ absorption coefficients at high
1127 pressure and high temperature. *Journal of Quantitative Spectroscopy & Radiative Transfer* 117, 21–28.

1128 Stofan, E. R., Smrekar, S. E., Mueller, N., Helbert, J., Jun. 2016. Themis Regio, Venus: Evidence for recent (?) volcanism
1129 from VIRTIS data. *Icarus* 271, 375–386.

1130 Stone, P. H., Jun. 1975. The dynamics of the atmosphere of Venus. *Journal of Atmospheric Sciences* 32, 1005–1016.

1131 Titov, D. V., Svedhem, H., Koschny, D., Hoofs, R., Barabash, S., Bertaux, J.-L., Drossart, P., Formisano, V., Häusler, B.,
1132 Korablev, O., Markiewicz, W. J., Nevejans, D., Pätzold, M., Piccioni, G., Zhang, T. L., Merritt, D., Witasse, O., Zender, J.,
1133 Accomazzo, A., Sweeney, M., Trillard, D., Janvier, M., Clochet, A., Nov. 2006. Venus Express science planning. *Planetary*
1134 *and Space Science* 54, 1279–1297.

1135 Tsang, C. C. C., Irwin, P. G. J., Taylor, F. W., Wilson, C. F., Apr. 2008. A correlated-k model of radiative transfer in the
1136 near-infrared windows of Venus. *Journal of Quantitative Spectroscopy and Radiative Transfer* 109, 1118–1135.

1137 Yamanoi, Y., Nakashima, S., Katsura, M., Jan. 2009. Temperature dependence of reflectance spectra and color values of
1138 hematite by in situ, high-temperature visible micro-spectroscopy. *American Mineralogist* 94, 90–97.

1139 Young, R. E., Walterscheid, R. L., Schubert, G., Seiff, A., Linkin, V. M., Lipatov, A. N., Sep. 1987. Characteristics of gravity
1140 waves generated by surface topography on Venus - Comparison with the VEGA Balloon results. *Journal of Atmospheric*
1141 *Sciences* 44, 2628–2639.